Accepted by ApJ on Oct. 4, 2019
Typeset using LaTeX **twocolumn** style in AASTeX62

Evolution of ONeMg Core in Super-AGB Stars towards Electron-Capture Supernovae: Effects of Updated Electron-Capture Rate

Shuai Zha,[1] Shing-Chi Leung,[2] Toshio Suzuki,[3,*] and Ken'ichi Nomoto[2]

[1] *Department of Physics, the Chinese University of Hong Kong, Hong Kong S. A. R., China*
[2] *Kavli Institute for the Physics and Mathematics of the Universe (WPI), The University of Tokyo Institutes for Advanced Study, The University of Tokyo, Kashiwa, Chiba 277-8583, Japan*
[3] *Department of Physics, College of Humanities and Sciences, Nihon University, Sakurajosui 3, Setagaya-ku, Tokyo 156-8550, Japan*

(Accepted by ApJ on October 4, 2019)

ABSTRACT

Stars with $\sim 8-10\ M_\odot$ evolve to form a strongly degenerate ONeMg core. When the core mass becomes close to the Chandrasekhar mass, the core undergoes electron captures on ^{24}Mg and ^{20}Ne, which induce the electron-capture supernova (ECSN). In order to clarify whether the ECSN leads to a collapse or thermonuclear explosion, we calculate the evolution of an 8.4 $M_\odot$ star from the main sequence until the oxygen ignition in the ONeMg core. We apply the latest electron-capture rate on ^{20}Ne including the second forbidden transition, and investigate how the location of the oxygen ignition (center or off-center) and the Y_e distribution depend on the input physics and the treatment of the semiconvection and convection. The central density when the oxygen deflagration is initiated, $\rho_{\rm c,def}$, can be significantly higher than that of the oxygen ignition thanks to the convection, and we estimate $\log_{10}(\rho_{\rm c,def}/{\rm g\ cm^{-3}}) > 10.10$. We perform two-dimensional simulations of the flame propagation to examine how the final fate of the ONeMg core depends on the Y_e distribution and $\rho_{\rm c,def}$. We find that the deflagration starting from $\log_{10}(\rho_{\rm c,def}/{\rm g\ cm^{-3}}) > 10.01 (< 10.01)$ leads to a collapse (thermonuclear explosion). Since our estimate of $\rho_{\rm c,def}$ exceeds this critical value, the ONeMg core is likely to collapse, although further studies of the convection and semiconvection before the deflagration are important.

Keywords: stars: evolution – hydrodynamics – supernovae: general

1. INTRODUCTION

A non-rotating solar-metallicity star with the zero-age-main-sequence mass ($M_{\rm ZAMS}$) in the range of $8-10\ M_\odot$ forms a strongly degenerate oxygen-neon-magnesium (ONeMg) core after the 2nd dredge up of the He layer (Nomoto 1984). Subsequently, the ONeMg core grows its mass through the H-He double shell burning and the star evolves along the super-asymptotic giant branch (SAGB) in the HR diagram. During the SAGB evolution, the H-rich envelope is losing its mass by various mechanisms such as a dust-driven wind, Mira-like pulsation, etc. (see a review by Höfner & Olofsson 2018). The fate of these stars is either the formation of an ONeMg white dwarf (WD) if almost all H-rich envelope is lost for $M_{\rm ZAMS} < M_{\rm up,Ne}$, or the electron-capture supernova (ECSN) if the ONeMg core mass reaches near the Chandrasekhar limit ($M_{\rm Ch}$) for $M_{\rm ZAMS} > M_{\rm up,Ne}$ (Nomoto et al. 1979; Miyaji et al. 1980; Nomoto 1984; Jones et al. 2013; Takahashi et al. 2013; Nomoto et al. 2013; Doherty et al. 2015). Here, $M_{\rm up,Ne}$ is the upper mass limit for the star which leaves behind an ONeMg WD (Nomoto et al. 2013). In the latter case, the ONeMg core undergoes various electron-capture and URCA processes.

Initiated by heating due to electron capture on ^{20}Ne, the oxygen *ignition* takes place in the central region (within ∼100 km of the center). Here the *ignition* is defined as the stage where the nuclear energy generation rate exceeds the thermal neutrino losses. We denote the central density at the oxygen ignition as $\rho_{\rm c,ign}$. Subsequently, oxygen burning grows into the thermonuclear runaway (when the timescale of temperature rise gets shorter than the dynamical timescale), and forms an oxygen deflagration wave behind which nuclear statistical equilibrium (NSE) is realized at temperature $T > 5\times10^9$ K. We denote the central density when the

* Visiting Researcher, National Astronomical Observatory of Japan, Mitaka, Tolyo 181-8588, Japan

oxygen deflagration starts as $\rho_{\rm c,def}$, which may be larger than $\rho_{\rm c,ign}$ if the convective energy transport after the oxygen ignition is efficient.

Further evolution of the ONeMg core depends on the competition between the nuclear energy release by the propagating oxygen deflagration wave and the reduction of the degeneracy pressure due to electron capture in the NSE ash behind the deflagration wave (Nomoto & Kondo 1991; Timmes & Woosley 1992; Jones et al. 2016; Leung & Nomoto 2019a).

Recent multi-dimensional simulations of the oxygen-deflagration have shown that the result of the above competition depends sensitively on the parameterized $\rho_{\rm c,def}$. If $\rho_{\rm c,def}$ is higher than a certain critical density $\rho_{\rm cr}$, the core collapses to form a neutron star (NS) because of the electron capture (Fryer et al. 1999; Kitaura et al. 2006; Radice et al. 2017). If $\rho_{\rm c,def} < \rho_{\rm cr}$, on the other hand, thermonuclear energy release dominates to induce the partial explosion of the ONeMg core (Jones et al. 2016).

For the critical density, $\log_{10}(\rho_{\rm cr}/{\rm g\ cm^{-3}}) = 9.90 - 9.95$ and $\log_{10}(\rho_{\rm cr}/{\rm g\ cm^{-3}}) = 9.95 - 10.3$ have been obtained by two-dimensional (2D) (Nomoto & Leung 2017a; Leung & Nomoto 2019a; Leung et al. 2019) and three-dimensional (3D) (Jones et al. 2016) hydrodynamical simulations, respectively. We should note that there still exists a big uncertainty in the treatment of the propagation of the oxygen deflagration (Timmes & Woosley 1992), as well as the electron-capture rates of the NSE composition (Seitenzahl et al. 2009) to obtain $\rho_{\rm cr}$.

We should also note that $\rho_{\rm c,def}$ is subject to uncertainties involved in the calculation of the final stages of the ONeMg core evolution (see below). $\log_{10}(\rho_{\rm c,def}/{\rm g\ cm^{-3}})$ is currently evaluated in the range of $9.9 - 10.2$ (Schwab et al. 2015, 2017a; Takahashi et al. 2019).

The uncertainties in the core evolution include: (1) the growth rate of the degenerate ONeMg core mass, which gives the rate of core contraction and compressional heating rate. This is determined by thermal pulses of He shell burning and the 3rd dredge-up, which require quite a lot of computational efforts. (2) Rates of URCA processes of ^{23}Na and ^{25}Mg, which cool down the core. (3) Electron-capture rates on ^{24}Mg and ^{20}Ne (Iben 1978; Jones et al. 2013; Schwab et al. 2015, 2017a). (4) The initial abundances of ^{24}Mg (Gutiérrez et al. 2005) and residual ^{12}C (Schwab & Rocha 2019) in the ONeMg core. (5) Treatment of the criterion for the convective stability (Paxton et al. 2018).

Most of the weak rates for these processes are theoretically calculated with the reliable *sd*-shell model until recently (Toki et al. 2013; Martínez-Pinedo et al. 2014) and provided with either analytic formulae or tables. However, there is still an uncertainty in the strength of the second-forbidden transition of ^{24}Mg and ^{20}Ne, which affects $\rho_{\rm c,def}$ substantially (Schwab et al. 2015).

Electron-capture processes not only reduce the electron number fraction (Y_e) but also heat the core through the energy deposition from γ-rays as well as distort the electron distribution function (e.g., Miyaji et al. 1980). Such heating makes the electron-capture front over-stable according to the Ledoux criterion and in the region of semiconvection (Miyaji & Nomoto 1987). Including semiconvection prescription proposed in Spruit (1992), Takahashi et al. (2019) found $\log_{10}(\rho_{\rm c,def}/{\rm g\ cm^{-3}}) \simeq 10.2$, while without any convection Schwab et al. (2017a) obtained $\log_{10}(\rho_{\rm c,ign}/{\rm g\ cm^{-3}}) \simeq 9.95$. Apart from altering $\rho_{\rm c,def}$, convection may enlarge the initial size of oxygen flame and change Y_e inside it, which can greatly affect the subsequent hydrodynamical behavior (Leung et al. 2019).

The newest electron-capture rate of ^{20}Ne including the second-forbidden transition (Kirsebom et al. 2018; Suzuki et al. 2019) can strongly affect how fast ^{20}Ne is converted to ^{20}F and the corresponding energy deposition. Such a heat source can alter the temperature profile and the convective structure of the core prior to the oxygen deflagration. So far there has not been much discussion on how this updated nuclear physics input affects the final fate of SAGB stars. Therefore, we calculated the detailed late-phase evolution of SAGB stars and modeled the subsequent propagation of the oxygen deflagration wave.

The structure of this paper is as follows. In Section 2, we present the evolutionary path of SAGB stars until the onset of the oxygen ignition, with the new weak rates and different convection criteria. In Section 3, we use 2D hydrodynamical simulations to model the oxygen deflagration phase through the collapse or explosion. We also discuss the dependence of the outcomes on the stellar evolution and other physical inputs. We summarize our results in Section 4.

2. EVOLUTION OF SAGB STARS

2.1. *Methods*

We evolve a non-rotating solar-metallicity star with $M_{\rm ZAMS} = 8.4\ M_\odot$ starting from the main-sequence phase, and follow the formation and growth of the degenerate ONeMg core until the ignition of oxygen burning, using Modules for Experiments in Stellar Astrophysics (MESA; Paxton et al. 2011, 2013, 2015, 2018, 2019), revision 8118. Until the formation of the ONeMg core, we use the MESA inlist of Jones et al. (2013). In short, the initial metallicity is $Z = 0.014$, the mixing-

length parameter 1.73 and the overshooting parameter $f_{\rm ov} = 0.014$ at all convective boundaries with the exception of $f_{\rm ov} = 0.005$ at the base of burning convective shells. Mass loss includes the Reimers prescription (Reimers 1975) for the RGB phase with $\eta = 0.5$ and the Blöcker prescription (Bloecker 1995) with $\eta = 0.05$ during the AGB phase. One difference is that we use the MESA nuclear reaction network `sagb_NeNa_MgAl.net` consisting of 22 isotopes to cover the H, He and C burning phases (Farmer et al. 2015). We add the important nuclear reaction ^{22}Ne$(\alpha, n)^{25}$Mg to produce the URCA cooling element ^{25}Mg (Kippenhahn et al. 2012, p. 203).

The modeling of the thermally pulsing AGB phase is computationally very expensive and numerical difficulties for modeling the thermal pulse and high temperature hydrogen ingestion make the calculation of the whole star up to the oxygen ignition impossible with current MESA (Schwab & Rocha 2019). There is a sharp density and temperature gradient at the interface between the degenerate ONeMg core and the H & He envelope, so they are in very loose contact with each other (see, Figure 15 of Nomoto 1984). The later evolution of the core is expected to be independent of the envelope except the mass accretion (Nomoto 1987; Takahashi et al. 2013). Therefore, when the degenerate ONeMg core of 1.28 $M_\odot$ is formed, we remove the envelope with an artificial mass loss rate ($0.1 - 1$ $M_\odot$ yr^{-1}). Nuclear burning during this phase is switched off for numerical simplicity. The resulting ONeMg core has a thin hot CO layer and is evolved to cool down until matter can be accreted. We checked that the cooling time (ranging from 1 yr to 1 Myr) does not affect the following evolution.

We model the ONeMg core growth phase until the oxygen ignition by assuming a constant mass accretion rate and the same accreted composition as the surface layer. The accretion rate is set to be 10^{-6} or 10^{-7} $M_\odot$ yr^{-1} to account for the uncertainties involved in the H-He double shell burning and the associated third dredge-up of the He layer (Doherty et al. 2017). The nuclear network further includes the URCA processes of ^{23}Na$\rightleftharpoons^{23}$Ne, ^{25}Mg$\rightleftharpoons^{25}$Na and ^{25}Na$\rightleftharpoons^{25}$Ne, and the electron-capture chains ^{24}Mg$(e^-,\nu_e)^{24}$Na$(e^-,\nu_e)^{24}$Ne and ^{20}Ne$(e^-,\nu_e)^{20}$F$(e^-,\nu_e)^{20}$O by using the state-of-the-art rate tables (provided by Toki et al. 2013; Suzuki et al. 2016). We consider the rate for the second forbidden transition of ^{20}Ne$(e^-,\nu_e)^{20}$F (Suzuki et al. 2019) as discussed in §2.2. The calculation is terminated when oxygen ignites in the mass zone with the maximum nuclear energy generation rate. Oxygen ignition is defined as when the nuclear energy generation rate by oxygen burning exceeds the thermal neutrino losses.

The semiconvection during electron capture is not accurately modeled with the mixing-length treatment in MESA, so we investigate the theoretical limits by using the two extreme criteria for the convective stability (Miyaji & Nomoto 1987; Kippenhahn et al. 2012). They are the Schwarzschild criterion:

$$\nabla_{\rm rad} < \nabla_{\rm ad}, \tag{1}$$

and the Ledoux criterion:

$$\nabla_{\rm rad} < \nabla_{\rm ad} + (\chi_{Y_e}/\chi_T)\nabla_{Y_e}. \tag{2}$$

Here, $\nabla_{\rm rad}$ and $\nabla_{\rm ad}$ are the radiative (assuming energy transport by only radiation and conduction) and adiabatic temperature gradients

$$\nabla_{\rm rad(ad)} \equiv \left(\frac{\partial \ln T}{\partial \ln P}\right)_{\rm rad(ad)}; \tag{3}$$

χ_{Y_e} and χ_T are the derivatives related to the equation of state

$$\chi_{Y_e} \equiv \left(\frac{\partial \ln P}{\partial \ln Y_e}\right)_T, \quad \chi_T \equiv \left(\frac{\partial \ln P}{\partial \ln T}\right)_{Y_e}; \tag{4}$$

and

$$\nabla_{Y_e} \equiv -\frac{d \ln Y_e}{d \ln P}. \tag{5}$$

The semiconvective region is treated as convectively unstable (stable) when using the Schwarzschild (Ledoux) criterion, although the growth timescale of overstability needs to be taken into account (Miyaji & Nomoto 1987).

2.2. *Electron-capture Rate of ^{20}Ne*

Here, we discuss the electron-capture rates on ^{20}Ne used in the present work, especially focusing on the forbidden transition, ^{20}Ne $(0^+_{\rm g.s.}) \rightarrow {}^{20}$F $(2^+_{\rm g.s.})$. Possible important roles of the forbidden transition in electron capture on ^{20}Ne was pointed out in Martínez-Pinedo et al. (2014). While the experimental transition rate was not well determined and only the lower limit of the log ft value was given for the second-forbidden β-decay transition ^{20}F $(2^+_{\rm g.s.}) \rightarrow {}^{20}$Ne $(0^+_{\rm g.s.})$, the transition was taken to be an allowed Gamow-Teller transition with B(GT) corresponding to the lower limit value of log ft =10.5; ft =6147/B(GT). Here, the GT transition strength B(GT) is defined by

$$B({\rm GT}) = \frac{(g_A/g_V)^2}{2J_i+1} \mid \langle f || \sum_k \vec{\sigma}^k \vec{t}^k_\pm || i \rangle \mid^2, \tag{6}$$

where g_A and g_V are the weak axial-vector and vector transition coupling constants, respectively; J_i is the total spin of the initial state; $\vec{\sigma}$ and $\vec{t}_\pm$ are the Pauli spin

matrix and isospin operator, respectively; $|i(f)\rangle$ is the initial (final) state. The β-decay rate λ at high density ρ and high temperature T can be expressed by using the ft value as

$$\lambda = \frac{f(\rho, T, \mu)}{ft} \ln 2, \quad (7)$$

where $f(\rho, T, \mu)$ with the electron chemical potential μ is the phase space factor for the transition (Fuller et al. 1980). As the rate λ is proportional to the transition strength B(GT) and the phase space factor $f(\rho, T, \mu)$, the ft value is given as ft =D/B(GT) with a constant D= $\frac{2\pi^3\hbar^7 \ln 2}{g_V^2 m_e^5 c^4}$ (m_e is electron mass) (Oda et al. 1994a; Langanke & Martínez-Pinedo 2001). But this prescription using a constant strength is an approximation.

Here, we treat the forbidden transition ^{20}Ne ($0^+_{\rm g.s.}$) $\rightarrow$ ^{20}F ($2^+_{\rm g.s.}$) properly, and evaluate the electron-capture rates by using the multipole expansion method (O'Connell et al. 1972; Walecka 1975, 1995). An explicit formula for the electron-capture rate for finite density and temperature is given, for example, in Paar et al. (2009) and Fantina et al. (2012). For a $0^+ \rightarrow 2^+$ transition, there are contributions from Coulomb, longitudinal and electric transverse terms induced by weak vector current as well as axial magnetic term induced by weak axial-vector current with multipolarity $J = 2$. Here J denotes the angular momentum transferred from the initial to the final states. Among them, about 60% contributions come from the Coulomb and longitudinal terms. The transition strength becomes electron energy dependent in contrast to the case of the prescription assuming an allowed transition. Note that the transition strengths or shape factors in forbidden transitions are energy dependent in general.

Calculated electron-capture rates for the forbidden transition obtained with the USDB Hamiltonian (Brown & Richter 2006) with and without the Coulomb effects are shown in Figure 1 for $\log_{10}(T/{\rm K}) = 8.6$. Screening effects on both electrons and ions are taken into account for the Coulomb effects (Juodagalvis et al. 2010; Toki et al. 2013; Suzuki et al. 2016). Here, the quenching factor q for the axial-vector coupling constant g_A is taken to be $q = 0.764$ (Richter et al. 2008). The Coulomb effects shift the electron-capture rates toward the higher density region due to an increase of the Q-value.

Recently, a new measurement for the β-decay ^{20}F ($2^+_{\rm g.s.}$) $\rightarrow$ ^{20}Ne ($0^+_{\rm g.s.}$) has been carried out, and the rate is determined to be log ft = 10.47±0.11 (Kirsebom et al. 2018), which is very close to the lower limit value log ft =10.5. Calculated rates obtained as an allowed transition with a B(GT) value corresponding to log ft =10.47 are also shown in Figure 1. The rates obtained with a constant B(GT) are found to be enhanced (reduced) compared with those with the USDB at $\log_{10}(\rho Y_e/{\rm g\ cm^{-3}}) < (>)$ 9.9 in case without the Coulomb effects. In case with the Coulomb effects, the former rates are enhanced compared with the latter at $9.6 < \log_{10}(\rho Y_e/{\rm g\ cm^{-3}}) < 9.9$ though the difference is smaller. These tendencies are due to the difference in the electron energy dependence of the transition strength between the two methods. The density dependence of the calculated rates with USDB by the multipole expansion method derived from energy dependent transition strength should be considered as more reliable than that obtained assuming an allowed transition. The Coulomb effects are non-negligible and the rates with the Coulomb effects obtained with USDB are recommended to be used in astrophysical calculations.

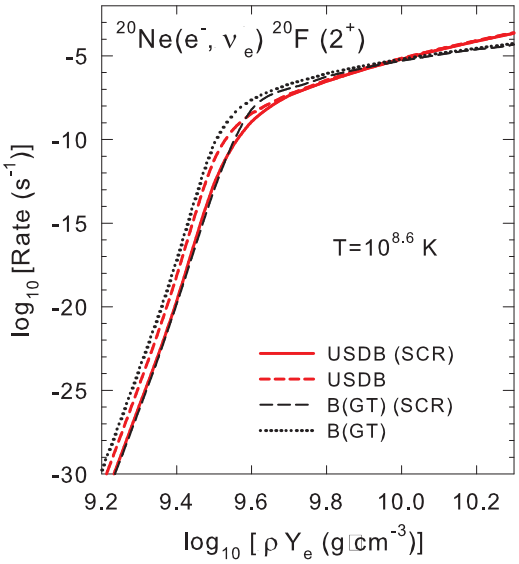

Figure 1. Calculated electron-capture rates for ^{20}Ne ($0^+_{\rm g.s.}$) $\rightarrow$ ^{20}F ($2^+_{\rm g.s.}$) obtained with the USDB Hamiltonian with and without the Coulomb (screening) effects for $\log_{10}(T/{\rm K}) = 8.6$. (SCR) in the legends denotes that the screening effects on electrons and ions are included. Calculated rates obtained as an allowed transition with a B(GT) value corresponding to log ft =10.47 for the inverse β-decay (Kirsebom et al. 2018) are also shown.

Total electron-capture rates on ^{20}Ne are shown in Figure 2. Contributions from Gamow-Teller transitions from $0^+_{\rm g.s.}$ and 2^+_1 states in ^{20}Ne to 1^+, 2^+ and 3^+ states in ^{20}F obtained with USDB are included as well as the forbidden transition, $0^+_{\rm g.s.} \rightarrow 2^+_{\rm g.s.}$.

2.3. *Evolution of ONeMg core up to electron capture on ^{24}Mg*

The evolution of the 8.4 $M_\odot$ star until the formation of the degenerate ONeMg core is similar to the lower mass models of Jones et al. (2013). Carbon is ignited

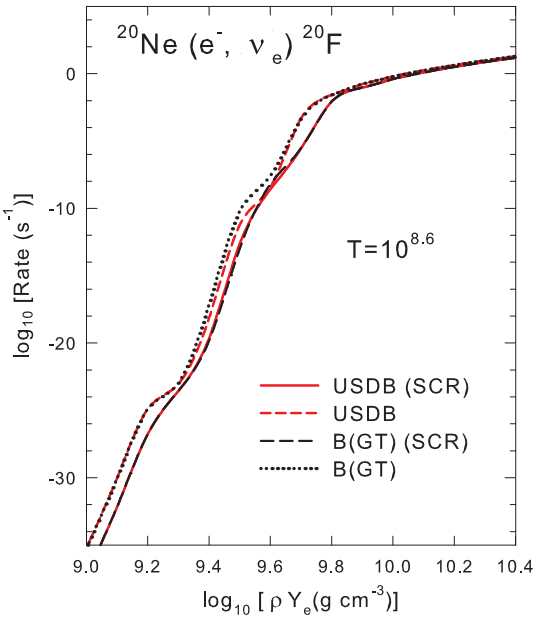

Figure 2. The same as in Figure 1 but for the total electron-capture rates for ^{20}Ne → ^{20}F at $\log_{10}$T(K) =8.6.

Table 1. Comparison for the key isotopic abundances of the ONeMg core in different studies. T13 stands for Takahashi et al. (2013), F15 for Farmer et al. (2015) and SQB17 for Schwab et al. (2017a).

Isotope	This work	T13	F15	SQB17
^{16}O	0.570	0.480	0.490	0.500
^{20}Ne	0.311	0.420	0.400	0.390
^{23}Na	0.069	0.035	0.060	0.050
^{24}Mg	0.031	0.050	0.030	0.050
^{25}Mg	0.010	0.015	0.002	0.010

slightly off-center at $M_r = 0.07\ M_\odot$ (M_r is the mass coordinate). The carbon burning shell steadily propagates to the center, similar to the off-center carbon flame models in Farmer et al. (2015). After we stop the evolution of the whole star and remove its envelope, an 1.28 $M_\odot$ core (with a $\sim 0.01\ M_\odot$ CO layer) is left behind with the abundance profile shown in Figure 3. The abundances of key isotopes for URCA process and electron capture are listed in Table 1 in comparison with other works (Takahashi et al. 2013; Farmer et al. 2015; Schwab et al. 2017a). The composition agrees well with Farmer et al. (2015) except we produce 1% ^{25}Mg with the addition of ^{22}Ne$(\alpha, n)^{25}$Mg. Note that we also find a residual carbon island at $M_r \lesssim 0.3\ M_\odot$, but the maximum abundance is only $\sim 1\%$ so that oxygen burning cannot be ignited by this residual carbon burning at $\log_{10}(\rho_c/\mathrm{g\ cm^{-3}}) < 9.8$ (Schwab & Rocha 2019).

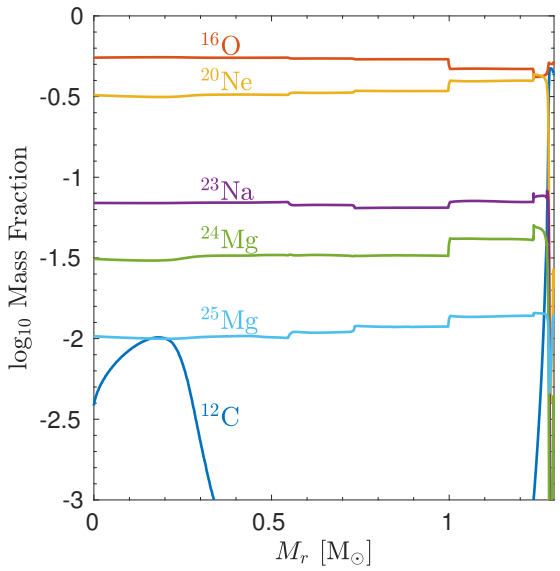

Figure 3. Composition profile of the degenerate ONeMg core of 1.28 $M_\odot$ evolved from a non-rotating solar-metallicity 8.4 $M_\odot$ star. The prescription for the evolution calculation with MESA was given in §2.1.

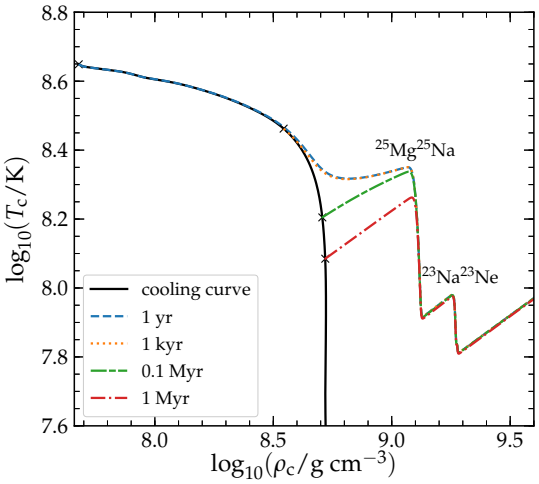

Figure 4. The evolution of the accreting ONeMg core in the central-density temperature plane after a range of cooling times. The black solid line is the cooling curve for the ONeMg core after removing the envelope, and the colored lines show the evolution after a cooling time of 1 yr, 1 kyr, 0.1 Myr and 1 Myr. The black crosses mark the starting points of the accretion. The results with different cooling times converge after the URCA cooling process by the ^{25}Mg^{25}Na pair at $\log_{10}(\rho_c/\mathrm{g\ cm^{-3}}) \simeq 9.1$.

After removing the envelope, the degenerate ONeMg core of 1.28 $M_\odot$ is evolved to cool down before the accretion starts. In Figure 4 we show the later evolution of the accreting core until $\log_{10}(\rho_c/\mathrm{g\ cm^{-3}}) = 9.6$, with the cooling time ranging from 1 yr to 1 Myr. The evolutionary paths undergo the same cooling due to the

^{25}Mg^{25}Na and ^{23}Na^{23}Ne URCA pairs irrespective of the earlier cooling. In other words, after the URCA cooling starts, the evolution does not depend on the earlier history.

For the accretion phase, until electron capture on ^{24}Mg takes place, no convective instability is expected for the central region (Schwab et al. 2017a). The thermal evolution of the core is dominated by the compressional heating, thermal neutrino losses and URCA cooling. Then, ^{24}Mg electron captures produce a negative temperature gradient and a positive Y_e gradient. The energy transport and mixing in such semiconvective region is not well constrained yet (Spruit 2013), so we use the two extreme stability criteria, i.e., the Schwarzschild and Ledoux criteria, for investigating the uncertainties. In the following, we discuss the evolution after ^{24}Mg$(e^-,\nu_e)^{24}$Na starts (when $\log_{10}(\rho_c/\mathrm{g\ cm^{-3}}) \simeq 9.6$) upon the usage of each criterion and set the theoretical uncertainty on the final outcomes.

2.4. *Evolution of ONeMg Core with Ledoux Criterion*

We first focus on the model with a mass accretion rate of $10^{-6}\ M_\odot\ \mathrm{yr}^{-1}$. When using the Ledoux criterion, the Y_e gradient is able to stabilize against convective instability during electron capture on ^{24}Mg. But after the onset of ^{24}Na$(e^-,\nu_e)^{24}$Ne, a convective core develops. Numerical difficulty occurs when this convective core grows to $\sim 0.055\ M_\odot$. The rapid change of the convective boundary cannot be resolved with the Newton iteration solver in MESA (Schwab et al. 2017a; Schwab & Rocha 2019). Two approaches are employed to further evolve the model. One is to mute the mixing-length theory treatment of convection by using the MESA option `mlt_option='none'` (model "L_no_mix"). Another is to limit the convection inside a mass coordinate $M_{\rm mix} = 0.05\ M_\odot$ beyond which we found the numerical difficulty (model "L_M_mix"). The evolution of the accreting ONeMg core in the central density-temperature plane is shown in Figure 5. The two approaches differ for the carbon ignition density, which is $\sim 2\%$ larger for L_M_mix due to the convective energy transport. Carbon burning does not ignite oxygen burning due to its low mass fraction in our ONeMg core model. Apart from this, the two models show the same evolution afterwards, as the thermal neutrino cooling drags the evolution back to a contractor (in balance between the compressional heating and thermal neutrino losses) at $\log_{10}(\rho_c/\mathrm{g\ cm^{-3}}) \simeq 9.8$ (Schwab & Rocha 2019).

Later, the central region is heated by the second forbidden transition of ^{20}Ne$(e^-,\nu_e)^{20}$F at $\log_{10}(\rho_c/\mathrm{g\ cm^{-3}}) \geq 9.8$ and cooled by the URCA process ^{25}Na$\leftrightharpoons^{25}$Ne at $\log_{10}(\rho_c/\mathrm{g\ cm^{-3}}) \approx 9.85$. The second forbidden transition is unable to ignite oxygen burning due to the slow increase of the electron-capture rate with respect to the density. The oxygen ignition then takes place mildly off-center at $M_r = 6\times10^{-4}\ M_\odot$ when $\log_{10}(\rho_c/\mathrm{g\ cm^{-3}}) \simeq 9.96$. The convective structure for the L_M_mix model is shown in Figure 6. A convectively unstable core is driven by ^{24}Na$(e^-,\nu_e)^{24}$Ne, until ^{24}Na is depleted in the central region at $\log_{10}(\rho_c/\mathrm{g\ cm^{-3}}) \simeq 9.75$. Heat released by electron capture on ^{20}Ne does not result in the convection of the core.

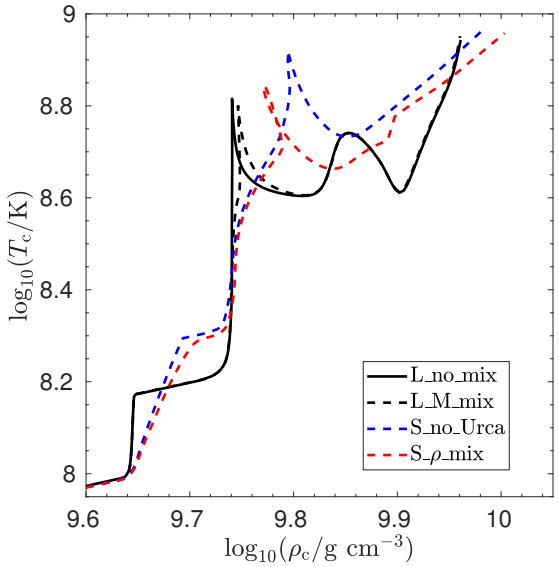

Figure 5. The evolution of the accreting ONeMg core in the central-density temperature plane for different treatments of the convection. 'L' stands for the Ledoux criterion and 'S' stand for the Schwarzschild criterion. The additional model nomenclature is explained in the main text.

2.5. *Evolution of ONeMg Core with Schwarzshild Criterion*

If we use the Schwarzschild criterion, the convection already emerges in the central region due to electron capture on ^{24}Mg. The convective core continues to grow and eventually reaches the layers with ongoing URCA process of ^{23}Na$\leftrightharpoons^{23}$Ne. Similar to Denissenkov et al. (2015) and Schwab et al. (2017b), the convective URCA process heats the core substantially in the MESA model. Due to this heating process, the core starts to expand at $\log_{10}(\rho_c/\mathrm{g\ cm^{-3}}) \simeq 9.7$. As the work done by convection to transport degenerate electrons to the high density region is not self-consistently taken into account, this heating could be artificial. For our purpose, we get rid of the convective URCA process by two means. One is to mute the URCA reactions when the convective core reaches the corresponding layers (model "S_no_URCA"). Another is to limit the convective core below the URCA cooling shells (model "S_ρ_mix"). The URCA process of

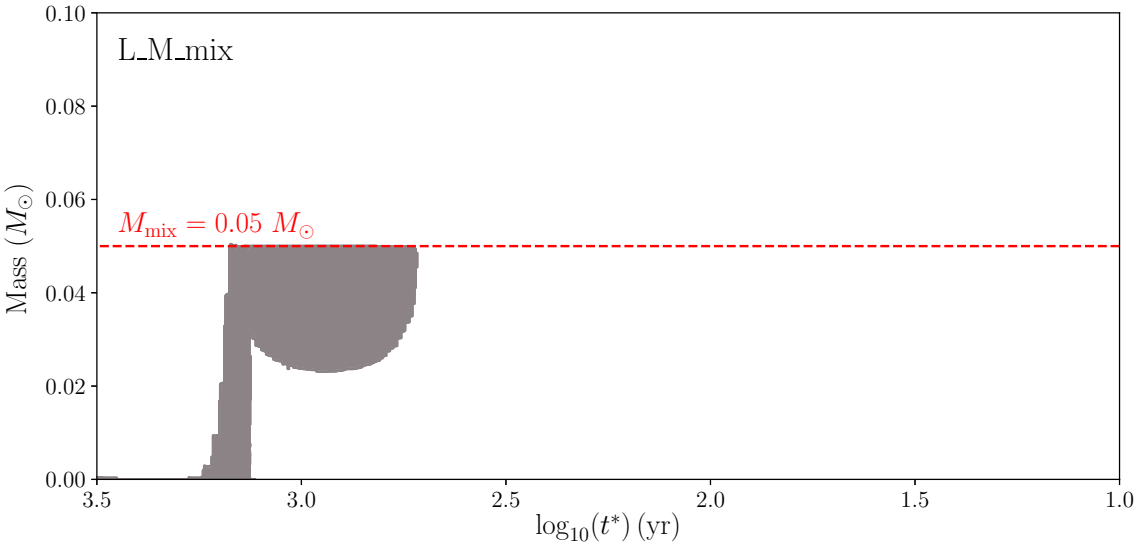

Figure 6. The Kippenhahn diagram for the accreting ONeMg core after the onset of electron capture on ^{24}Mg. The gray shaded areas are convectively unstable. t^* is the time left before the end of the calculation. The Ledoux criterion is used for the convective stability and convection is allowed only inside 0.05 $M_\odot$ to avoid numerical difficulties. A convectively unstable core is driven by $^{24}\mathrm{Na}(e^-,\nu_e)^{24}\mathrm{Ne}$, until ^{24}Na is depleted in the central region at $\log_{10}(\rho_{\rm c}/\mathrm{g\ cm^{-3}}) \simeq 9.75$. Later, the core remains convectively stable until oxygen burning is ignited.

$^{25}\mathrm{Na}\leftrightharpoons{}^{25}\mathrm{Ne}$ is muted as its threshold density is higher than that of $^{24}\mathrm{Mg}(e^-,\nu_e)^{24}\mathrm{Na}$.

Evolution of the accreting ONeMg core in the central density-temperature plane is also shown in Figure 5, in comparison with the Ledoux models. In this case, electron capture processes always make the core convectively unstable and the temperature increases slowly but to a higher value as more fuel is mixed into the center. Carbon burning is ignited at $\log_{10}(\rho_{\rm c}/\mathrm{g\ cm^{-3}}) \simeq 9.8$ and cannot ignite oxygen burning. Convective structure of these two models are shown in Figures 7 and 8. An extended convective core is found in both models and has a mass of 0.74 $M_\odot$ and 0.66 $M_\odot$ at the oxygen ignition.

2.6. *Oxygen Ignition*

As seen in Figure 5, the contraction of the ONeMg core eventually leads to the oxygen ignition at $\log_{10}(T/K) \approx 9.0$. For the Schwarzshild criterion, due to the convective energy transport, the oxygen ignition takes place at the center and is delayed to a higher central density than that of the Ledoux models.

We compare the temperature and Y_e profiles at the oxygen ignition for the above 4 models in Figure 9. The temperature profile is determined by heating due to the electron capture and compression, cooling due to the thermal and URCA neutrino losses, and the energy transport.

For the Ledoux criterion, the result with allowing the convection at $M_r < M_{\rm mix} = 0.05\ M_\odot$ is identical to that with convection suppressed. The temperature profile is super-adiabatic at the central region stabilized by the positive Y_e gradient. As the electron capture on ^{24}Mg takes place at $M_r \sim 0.1\ M_\odot$, its heating results in another temperature inversion there. The temperature drops at $M_r \lesssim 0.1\ M_\odot$ due to the thermal neutrino losses and falls off rapidly at $M_r \gtrsim 0.1\ M_\odot$ due to the rapid decrease of the electron capture rate below the threshold density. There is also a sharp Y_e rise at $M_r \sim 0.1\ M_\odot$ corresponding to the ^{24}Mg electron capture front.

The two models with the Schwarzschild criterion have a similar central temperature structure except that the convective core is more extended in S_ρ_mix. The temperature profile is adiabatic because of the efficient convective energy transport. Both models have a homogeneous Y_e profile in the central convective region. The key parameters for these models are summarized in Table 2 as the inputs for the subsequent hydrodynamical simulations.

2.6.1. *Off-center Oxygen Ignition*

We found that with the inclusion of the second forbidden transition for $^{20}\mathrm{Ne}(e^-,\nu_e)^{20}\mathrm{F}$ and using the Ledoux criterion, the oxygen ignition starts slightly off-center. This behavior was found to lower the critical $\rho_{\rm c,def}$ below which the star explodes instead of collapsing (Leung et al. 2019). To address the reason for this off-center ignition, we show the evolution of the mass fractions of ^{20}Ne and temperature as a function of the increasing local density for 4 representative mass zones in Figure 10.

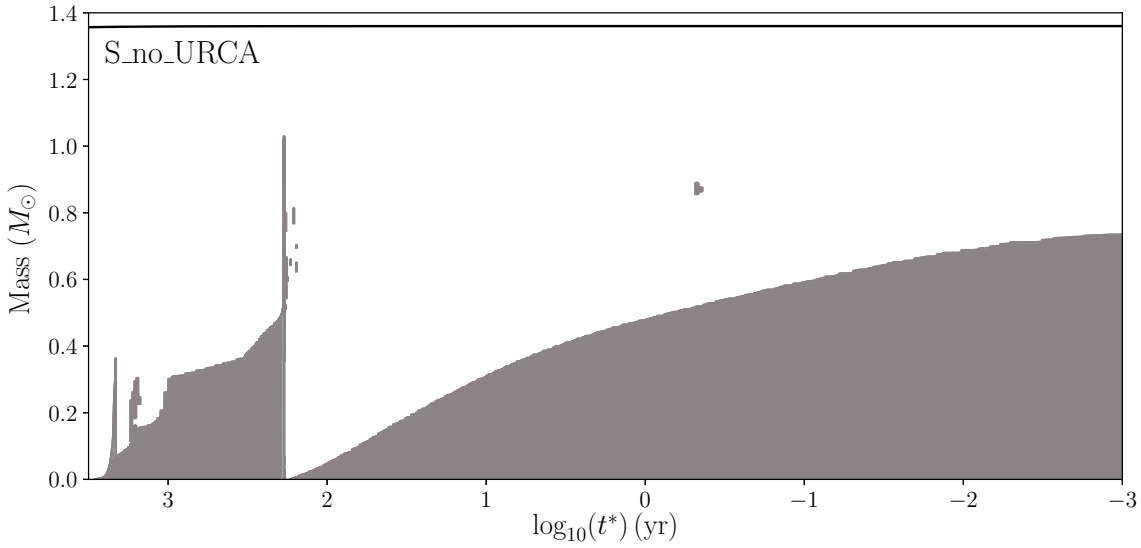

Figure 7. Same as Figure 6, but the Schwarzschild criterion is used for the convective stability and URCA processes are muted. When oxygen burning is ignited, the convective core grows to $\sim 0.74\ M_\odot$.

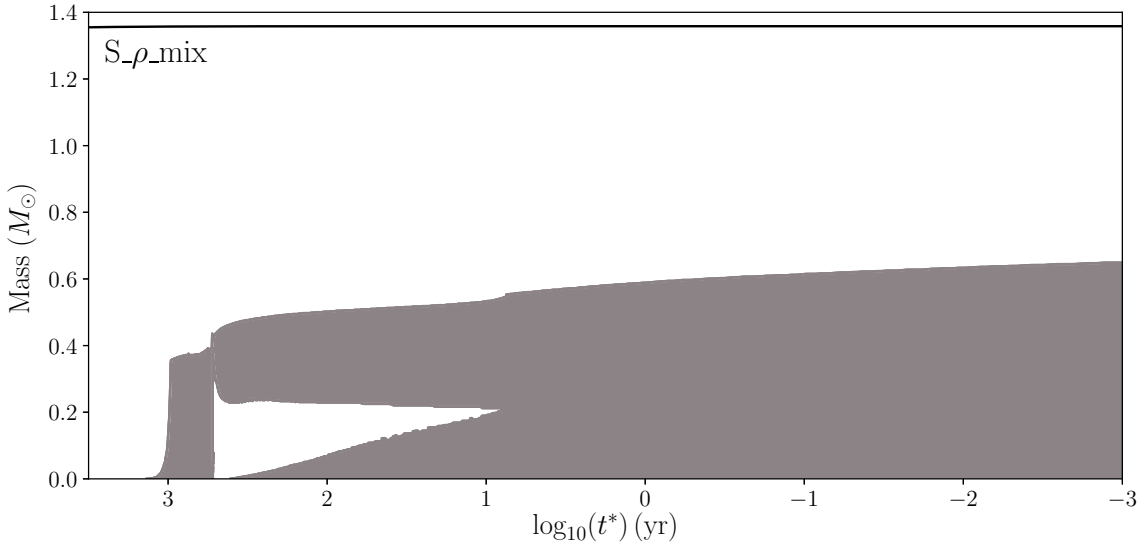

Figure 8. Same as Figure 6, but the Schwarzschild criterion is used for the convective stability and the convective core is limited below the URCA cooling shells. When oxygen burning is ignited, the convective core grows to $\sim 0.66\ M_\odot$.

The oxygen ignition takes place at $M_r = 6 \times 10^{-4}\ M_\odot$. During accretion, the core is compressed and the densities in the mass zones increase, so the density can be used as a metric for time as indicated by arrows in Figure 10. When reaching the same density, the outer zones has a larger ^{20}Ne fraction than the innermost zone. This means that electron capture on ^{20}Ne is slower for the outer zones than the innermost zone ('center' in Figure 10). The higher ^{20}Ne fraction in the outer zone results in a larger heating effect and temperature inversion. As a result, the oxygen ignition takes place mildly off-center.

2.6.2. *Dependence on Core Growth Rate*

To test the uncertainty of progenitor properties involved in the mass growth process, we calculate another set of models with a mass accretion rate of $10^{-7}\ M_\odot\ \mathrm{yr}^{-1}$. The key parameters for the models at the oxygen ignition are also listed in Table 2. Most of the results show negligible differences compared to those with $10^{-6}\ M_\odot\ \mathrm{yr}^{-1}$, except that for the case without

Table 2. Key parameters for the profiles at the oxygen ignition for different models, with a mass accretion rate ($\dot{M}$) of 10^{-6} or 10^{-7} $M_\odot$ yr^{-1}. $\rho_{\rm c,ign}$ is the central density at the oxygen ignition and $Y_{e,\rm ign}$ the electron fraction at the ignited mass zone. $M_{\rm conv}$ and $M_{\rm final}$ are the masses of the convective core and whole ONeMg core, respectively. $r_{\rm ign}$ and $M_{r,\rm ign}$ are respectively the radial position and mass coordinate of the oxygen ignited zone, and 0 indicates the central ignition.

$\dot{M}$ [$M_\odot$ yr^{-1}]	Model	$\log_{10}(\rho_{\rm c,ign}/{\rm g\ cm^{-3}})$	$Y_{e,\rm ign}$	$M_{\rm conv}$ [$M_\odot$]	$M_{\rm final}$ [$M_\odot$]	$r_{\rm ign}$ [km]	$M_{r,\rm ign}$ [$M_\odot$]
10^{-6}	L_no_mix	9.96	0.464	—	1.361	32	0.6×10^{-3}
	L_M_mix	9.96	0.464	—	1.361	32	0.6×10^{-3}
	S_no_URCA	9.98	0.491	0.74	1.360	0	0
	S_ρ_mix	10.00	0.489	0.66	1.358	0	0
10^{-7}	L_no_mix	9.97	0.466	—	1.359	61	4.4×10^{-3}
	S_no_URCA	9.98	0.491	0.80	1.358	0	0
	S_ρ_mix	10.00	0.489	0.66	1.357	0	0

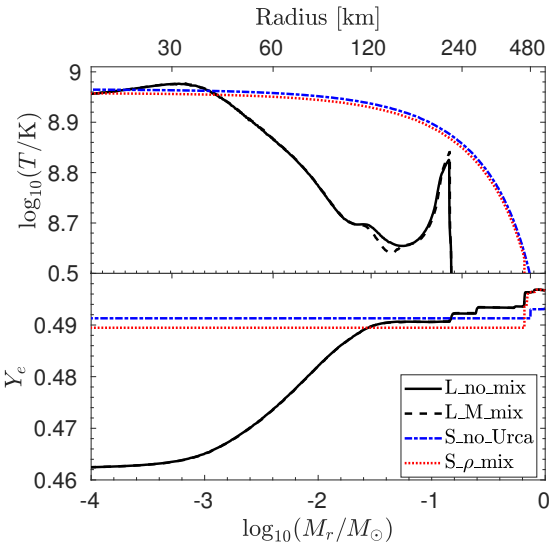

Figure 9. Temperature (top panel) and Y_e (bottom panel) profiles at the oxygen ignition for the 4 models with different treatments of the convection. The two models with the Ledoux criterion, i.e., L_no_mix and L_M_mix, overlap with each other.

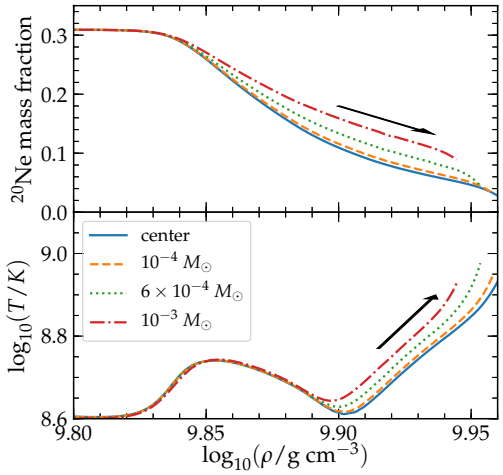

Figure 10. The evolution of the mass fraction of ^{20}Ne (the upper panel) and temperature (the lower panel) as a function of the increasing local density for 4 mass zones for the model "L_no_mix" with the 'Kunz' rate for $^{12}{\rm C}(\alpha,\gamma)^{16}{\rm O}$ and the core growth rate of 10^{-6} $M_\odot$ yr^{-1}. Here, the density is used as a metric for time as indicated by the arrow.. The oxygen ignition takes place at $M_r = 6\times10^{-4}$ $M_\odot$.

any convection (L_no_mix), the oxygen ignition takes place further off-center at 61 km.

2.6.3. *Location of Oxygen Ignition and ^{20}Ne Mass Fraction*

There is still an uncertainty for the reaction rate of $^{12}{\rm C}(\alpha,\gamma)^{16}{\rm O}$ (An et al. 2016). It is difficult to measure the rate at energies relevant for astrophysics. This rate affects the relative abundance of ^{12}C and ^{16}O after He burning, thus affecting the mass fraction of ^{20}Ne $X(^{20}{\rm Ne})$ after carbon burning. We check how this uncertainty affects our results by using three available rates for $^{12}{\rm C}(\alpha,\gamma)^{16}{\rm O}$ in the MESA code. In the previous models, we use 'Kunz' (Kunz et al. 2002), which results in $X(^{20}{\rm Ne}) = 0.311$. The other rates are 'jina reaclib' (Cyburt et al. 2010) and 'CF88' (Caughlan & Fowler 1988)[1], which result in $X(^{20}{\rm Ne}) = 0.325$ and $X(^{20}{\rm Ne}) = 0.296$, respectively.

In Figure 11 we compare the final temperature profiles for the three $^{12}{\rm C}(\alpha,\gamma)^{16}{\rm O}$ rates. The convection is suppressed as in the 'L_no_mix' model. Table 3 summarizes $X(^{20}{\rm Ne})$ and $X(^{16}{\rm O})$ before and after electron capture on ^{20}Ne and the location of the oxygen ignition. Although the difference in $X(^{20}{\rm Ne})$ is relatively small, the ignition position of oxygen burning is different. In particular, for the largest $X(^{20}{\rm Ne})$ with the 'jina reaclib' rate, the oxygen ignition takes place at the center.

[1] The CF88 rate in MESA is larger than the original rate by a factor of 1.7.

Table 3. Dependence of stellar evolution results on the $^{12}C(\alpha,\gamma)^{16}O$ rate. We used three options for the $^{12}C(\alpha,\gamma)^{16}O$ rates in the MESA code: 'Kunz' (Kunz et al. 2002) , 'jina reaclib' (Cyburt et al. 2010) and 'CF88' (Caughlan & Fowler 1988). X_i is the initial mass fraction of the relevant element. $X_{c,f}$ and $X_{ign,f}$ are the final mass fractions of the relevant element in the central and oxygen ignited zones, respectively. r_{ign} and $M_{r,ign}$ are the radial position and mass coordinate of the oxygen ignited zone.

Rate option	$X_i(^{20}Ne)$	$X_i(^{16}O)$	$X_{c,f}(^{20}Ne)$	$X_{ign,f}(^{20}Ne)$	r_{ign} [km]	$M_{r,ign}$ [$M_\odot$]
Knuz	0.311	0.570	0.026	0.039	32	0.6×10^{-3}
jina reaclib	0.325	0.549	0.036	0.036	0	0
CF88	0.296	0.595	0.018	0.043	45	1.8×10^{-3}

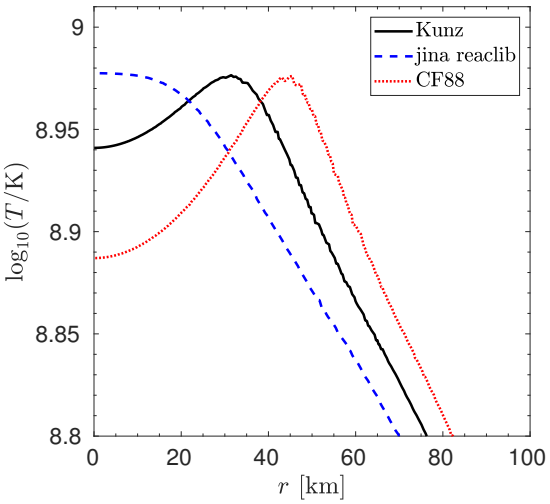

Figure 11. Comparison of the temperature profiles at the oxygen ignition for different $^{12}C(\alpha,\gamma)^{16}O$ rates. The temperature peak indicates the oxygen ignition site. For the model with the 'jina reaclib' rate, the mass fraction of ^{20}Ne is large enough to result in the central ignition. The 'CF88' rate gives the lowest ^{20}Ne fraction, and so the ignition site has the largest distance from the center.

For the smallest $X(^{20}Ne)$ with the 'CF88' rate, the ignition takes place further off-center at $r_{ign} = 45$ km. The difference in the ignition position affects the final outcome of the hydrodynamical phase, which is explored in Section 3.

2.6.4. *Effects of Residual Carbon*

In the ONeMg core, there is a trace amount of residual carbon (Schwab & Rocha 2019). In our case, the $\sim 1\%$ carbon is not enough to ignite oxygen burning at low density even if no mixing is allowed. However, Schwab & Rocha (2019) showed that with $\sim 3\%$ residual carbon (in a lower M_{ZAMS} star) and without mixing, oxygen burning is ignited at $\log_{10}(\rho_{c,ign}/\mathrm{g\ cm^{-3}}) \sim 9.7$. It is important to investigate how the convective mixing affects the results for this high carbon abundance as well as the convective URCA process associated with the carbon burning.

2.7. *From Oxygen Ignition to Deflagration*

We stop the MESA calculations at the oxygen ignition when the energy generation rate by oxygen burning exceeds thermal neutrino losses at the mass zone with the maximum energy generation rate. At this state, the heating timescale by the local oxygen burning is estimated as

$$\tau_{burn\_o} = c_p T/\varepsilon_{burn\_o} \tag{8}$$

where c_p is the specific heat at constant pressure and ε_{burn_o} the nuclear energy generation rate of oxygen burning. At the oxygen ignition, τ_{burn_o} is $\sim 10^{7-8}$ s, which is still 8-9 orders of magnitude larger than the dynamical timescale (~ 0.04 s at $\log_{10}(\rho/\mathrm{g\ cm^{-3}}) = 10$). Thus the thermonuclear runaway of local oxygen burning does not take place yet.

Oxygen burning forms a convectively unstable region even for the Ledoux criterion. The convective region will develop above the oxygen burning region, which is numerically difficult to calculate with the current MESA code. The further evolution is estimated as follows.

Firstly, materials in the convective region will be mixed. For the Schwarzschild models, the convective mixing from the center due to oxygen burning does not make much change of the T and Y_e profiles seen in Figure 9.

For the L_no_mix model, Y_e in the mixed region will become much higher than 0.46. If the convective region extends to $M_r \sim 0.14\ M_\odot$, Y_e becomes ~ 0.49 as estimated from the black solid line in Figure 9. As a result, only the very small central region of $M_r < 6\times10^{-4} M_\odot$ will have $Y_e \simeq 0.46$, while the outer part will have $Y_e \sim 0.49$. Except for the very small central region, the averaged T and Y_e profiles may not be so different from the Schwarzschild cases.

Secondly, for all models, the timescale of the temperature rise in the burning region will become long by the convective energy transport. Then the ONeMg core will continue to rapidly contract because of electron capture in the core whose mass is close to the "effective" M_{Ch} with low Y_e. During contraction, the evolution in $\log_{10}\rho - \log_{10} T$ of the burning shell for all cases in Figure 5 will be close to the S_ρ_mix model (red dashed line) because of the convective energy transport. Eventually, the temperature reaches $\log_{10}(T/\mathrm{K}) \sim 9.3$ where

the thermonuclear runaway occurs. To estimate $\rho_{\rm c,def}$ at the runaway, we extrapolate the evolutionary paths of the burning shell of all cases along the red dashed line of S_ρ_mix in Figure 5 from the oxygen ignition to $\log_{10}(T/{\rm K}) \sim 9.3$. We obtain $\log_{10}(\rho_{\rm c,def}/{\rm g\ cm^{-3}}) \approx 10.18$ even for the off-center ignition case. This is consistent with $\log_{10}(\rho_{\rm c,def}/{\rm g\ cm^{-3}}) \simeq 10.2$ found by Takahashi et al. (2019), who took into account the semiconvective mixing. (If the super-adiabatic temperature gradient is taken into account, the runaway density would be a little lower.)

Because of the uncertainty in the evolution from the oxygen ignition through the thermonuclear runaway, in Section 3 we use the initial models with parameterized Y_e distribution and $\rho_{\rm c,def}$ to study the parameter dependence of the hydrodynamical behavior. For the central density, we adopt $\log_{10}(\rho_{\rm c,def}/{\rm g\ cm^{-3}}) = 9.96 - 10.2$. For the Y_e distribution, we adopt three cases as will be described in §3.2 and shown in Figure 12.

3. HYDRODYNAMICAL SIMULATIONS OF ELECTRON-CAPTURE SUPERNOVAE

3.1. *Methods*

We use a 2D hydrodynamics code primarily developed for the supernova modeling (Leung et al. 2015a). The code has been applied to study Type Ia supernova (Leung et al. 2015b; Nomoto & Leung 2017b; Leung & Nomoto 2018, 2019b), accretion-induced collapse (Leung et al. 2019; Zha et al. 2019) and ECSN (Nomoto & Leung 2017a; Leung & Nomoto 2019a). Here we briefly review the algorithms particularly relevant to the modeling of ECSN. We refer the interested readers to the detailed implementation reported in Leung et al. (2019).

The code solves the 2D Euler equations using the fifth-order WENO scheme for spatial discretization (Barth & Deconinck 1999) and five-step third-order NSSP Runge-Kutta scheme for time discretization (Wang & Spiteri 2007). We use the Helmholtz equation of state (Timmes & Arnett 1999). For the propagation speed of the oxygen deflagration, we implement sub-grid scale turbulence models introduced in Clement (1993) and Niemeyer & Hillebrandt (1995), with the turbulent flame model given in Pocheau (1994), Reinecke et al. (1999a, 2002) and Schmidt et al. (2006). We use the laminar flame speed as a function of the density and composition given in Timmes & Woosley (1992). To capture the geometry of oxygen deflagration we use the level-set method (Reinecke et al. 1999b) with reinitialization (Sussman et al. 1994). We use the three-step nuclear reaction to represent the energy production by nuclear burning (Townsley et al. 2007; Calder et al. 2007). Effects of binding energy changes, neutrino energy losses

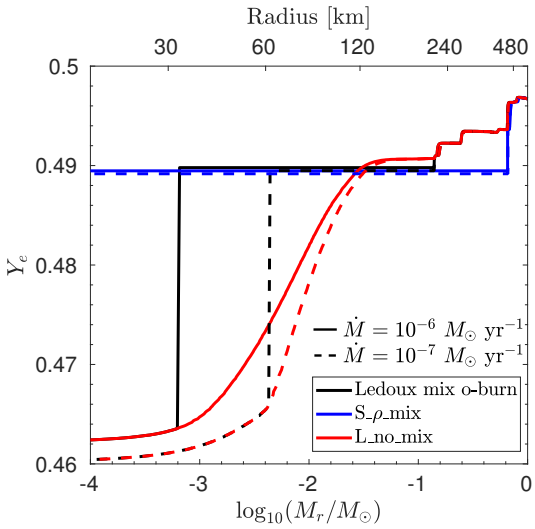

Figure 12. Y_e profiles for the construction of initial models for the hydrodynamical simulations, with different assumptions of the convective mixing as described in §3.2. The solid (dashed) lines are with $\dot{M} = 10^{-6}$ (10^{-7}) $M_\odot$ yr^{-1}. In the Ledoux models, the position of the oxygen ignition is $r_{\rm ign} = 32$ (61) km and $M_r = 0.6 \times 10^{-3}$ (4.4×10^{-3}) $M_\odot$ for $\dot{M} = 10^{-6}$ (10^{-7}) $M_\odot$ yr^{-1}.

and mass differences between electron-proton pair and neutron are included for matter in NSE. The individual electron-capture rates of isotopes in the NSE ash are taken from Fuller et al. (1985); Oda et al. (1994b); Martínez-Pinedo & Langanke (1999); Nabi & Klapdor-Kleingrothaus (1999).[2]

We start the hydrodynamical phase of evolution by mapping the MESA model onto a 2D grid in cylindrical coordinates with a uniform spatial resolution of $\Delta x \approx 4$ km. (Details of the initial models are described in the §3.2.) To trigger the initial flame, we consider a central flame of a "three-finger" structure (see a similar illustration in Reinecke et al. 1999a) and an off-center flame with a one-bubble structure (also see Reinecke et al. 1999a). The bubble is put at $r_{\rm ign} = 30$ or 60 km away from the center[3]. The initially ignited matter is assumed to be burnt into NSE. A typical mass of

[2] We remark that the computation of the electron-capture rate is still uncertain because the rate table for matter in NSE with $Y_e \leq 0.4$ relies on multiple tables. In particular, rates for isotopes with the mass number $A = 45 - 110$ are based on Nabi & Klapdor-Kleingrothaus (1999). These rates have been calculated in Juodagalvis et al. (2010) based on the more sophisticated large-scale shell model as in (see e.g. Langanke & Martínez-Pinedo 2000) but the actual values are unavailable yet.

[3] The location of the oxygen ignition is $r_{\rm ign} = 32$ (61) km from the stellar evolutionary models with $\dot{M} = 10^{-6}$ (10^{-7}) $M_\odot$ yr^{-1}. For the hydrodynamical simulations, the results are not sensitive to the exact values for the adopted finite grid resolution.

Table 4. The initial configuration and the final fate of the representative models studied in this work. The model series names "S_ρ_mix" and "L_no_mix" respectively stand for the initial models obtained from the stellar evolution calculations where the the Schwarzschild and Ledoux criteria are used for the convection criterion. "Ledoux mix o-burn" stands for the initial models calculated with the Ledoux criterion including the convective shell mixing due to the off-center oxygen ignition. In "Conv. (Convection)", "S" and "L" stand for the Schwarzschild and Ledoux criteria, respectively, being used in the stellar evolution calculations. In "Mix. (Mixing)", "Y" means the convective mixing is included in setting the initial Y_e profile in the convective zone of "S_ρ_mix" and "Ledoux mix o-burn", while "N" means no mixing is assumed after the oxygen ignition for "L_no_mix". "Y_e" is the initial value at the center for "S_ρ_mix" and "L_no_mix", while it is the value in the off-center convective zone for "Ledoux mix o-burn". The model name with an ending " -LM" makes it clear that the convective mixing after the oxygen ignition is included in "Ledoux mix o-burn". The initial central density $\rho_{\rm c,def}$ is in units of g cm^{-3}. Radius R and initial flame position $r_{\rm ign}$ are in units of km. Mass M is in unit of $M_\odot$. $\dot{M}$ is the progenitor mass accretion rate in units of $M_\odot$ yr^{-1}. "Result" stands for the final fate with "C" being collapse and "E" being explosion.

Model	$\dot{M}$	$\log_{10}(\rho_{\rm c,def})$	M	R	$r_{\rm ign}$	Y_e	Conv.	Mix.	Result
Ledoux mix o-burn									
6-0998-049-30-LM	10^{-6}	9.98	1.359	1400	30	0.49	L	Y	E
6-0999-049-30-LM	10^{-6}	9.99	1.359	1410	30	0.49	L	Y	C
6-1000-049-30-LM	10^{-6}	10.00	1.359	1420	30	0.49	L	Y	C
7-1000-049-60-LM	10^{-7}	10.00	1.357	1370	60	0.49	L	Y	E
7-1002-049-60-LM	10^{-7}	10.02	1.358	1350	60	0.49	L	Y	C
S_ρ_mix									
6-0996-049-00	10^{-6}	9.96	1.359	1410	0	0.49	S	Y	C
6-0996-049-30	10^{-6}	9.96	1.359	1410	30	0.49	S	Y	C
6-1000-049-00	10^{-6}	10.00	1.360	1370	0	0.49	S	Y	C
6-1000-049-30	10^{-6}	10.00	1.360	1370	30	0.49	S	Y	C
7-0997-049-00	10^{-7}	9.97	1.358	1410	0	0.49	S	Y	C
7-0997-049-60	10^{-7}	9.97	1.358	1410	60	0.49	S	Y	E
7-0999-049-60	10^{-7}	9.99	1.359	1360	60	0.49	S	Y	C
7-1000-049-00	10^{-7}	10.00	1.360	1370	0	0.49	S	Y	C
7-1000-049-60	10^{-7}	10.00	1.360	1370	60	0.49	S	Y	C
L_no_mix									
6-0996-046-30	10^{-6}	9.96	1.357	1430	30	0.46	L	N	E
6-0996-046-00	10^{-6}	9.96	1.357	1430	0	0.46	L	N	E
6-0996-046-00b[a]	10^{-6}	9.96	1.357	1430	0	0.46	L	N	C
6-1000-046-30	10^{-6}	10.00	1.357	1400	30	0.46	L	N	E
6-1000-046-00	10^{-6}	10.00	1.357	1400	0	0.46	L	N	C
6-1010-046-30	10^{-6}	10.10	1.361	1310	30	0.46	L	N	C
7-0997-046-00	10^{-7}	9.97	1.355	1430	0	0.46	L	N	E
7-0999-046-00	10^{-7}	9.99	1.356	1380	0	0.46	L	N	E
7-1000-046-00	10^{-7}	10.00	1.357	1400	0	0.46	L	N	C
7-0997-046-60	10^{-7}	9.97	1.355	1430	60	0.46	L	N	E
7-1000-046-60	10^{-7}	10.00	1.357	1400	60	0.46	L	N	E
7-1002-046-60	10^{-7}	10.02	1.357	1360	60	0.46	L	N	E
7-1005-046-60	10^{-7}	10.05	1.358	1330	60	0.46	L	N	C

[a]The flame size is two times larger

$\sim 10^{-4}$ to 10^{-3} $M_\odot$ for the initial ash is assumed. In all simulations, we follow the propagation of the oxygen deflagration wave until the ONeMg core reaches a central density of $\log_{10}(\rho_c/\mathrm{g\ cm^{-3}}) = 10.7$ (9.0) for the collapse (explosion) case.

3.2. *Initial Models*

In building the initial models in the hydrostatic equilibrium at the initiation of the deflagration, we use the stellar evolutionary models with $\dot{M} = 10^{-6}$ $M_\odot$ yr^{-1} and 10^{-7} $M_\odot$ yr^{-1}. We use the ^{12}C$(\alpha,\gamma)^{16}$O rates by 'Kunz' (Table 2) and also 'jina_reaclib' (Table 3) to include the case of the central oxygen ignition.

For the Y_e and temperature profiles, we take into account the dependence on the convection criteria as shown in Figure 9 and Table 2. We also take into account the convection which develops after the oxygen ignition even for the Ledoux criterion (§2.7). The convection mixes the high Y_e matter in the outer part of the ONeMg core with the low Y_e materials at the oxygen-burning site (center or off-center).

Therefore, for the initial Y_e profile, we constructed the following 3 cases (1)-(3) shown in Figure 12. We examine the dependence of the final fate of the ONeMg core on these initial Y_e distributions in §3.3 - 3.5. More details on the configuration are described in each subsection.

(1) "Ledoux mix o-burn": L_no_mix + mixed region above the oxygen ignited shell (§3.3).

(2) "S_ρ_mix": Schwarzshild criterion with almost full mixing. This also accounts for the convective mixing after the central ignition due to the usage of the 'jina_reaclib' rate for the Ledoux criterion (§3.4).

(3) "L_no_mix": Ledoux criterion with no mixing (§3.5).

In these models, $\rho_{\rm c,def}$ is a model parameter. As discussed in §2.7, the convective energy transport above the oxygen ignited shell can significantly delay the thermonuclear runaway, thus increasing $\rho_{\rm c,def}$. However, the exact details of the convective energy transport and mixing remain unknown due to numerical difficulties with MESA. Therefore, the exact $\rho_{\rm c,def}$ when the deflagration starts and its position are not well determined. As estimated in §2.7, $\log_{10}(\rho_{\rm c,def}/\mathrm{g\ cm^{-3}})$ can be as high as 10.18. Here we take $\log_{10}(\rho_{\rm c,def}/\mathrm{g\ cm^{-3}})$ ranging from 9.96 to 10.2.

We do not directly map the MESA density profile because we find that the discretization produces global motion of the ONeMg core, which may affect the initial propagation of the flame and the final fate. Instead, we recalculate the hydrostatic equilibrium explicitly for a central density $\rho_{\rm c,def}$, with Y_e and temperature as a function of M_r.

In Table 4 we tabulate the parameters and the outcomes of the hydrodynamical simulations for the models studied in this work. We name the models as follows. In 6-0996-046-30, 7-1002-049-60, and 6-0998-049-30-LM,, for example,

(a) "6" and "7" stand for the "6"-series and "7"-series progenitors evolved with $\dot{M} = 10^{-6}$ $M_\odot$ yr^{-1} and 10^{-7} $M_\odot$ yr^{-1}, respectively.

(b) "0996", "0998" and "1002" stand for $\log_{10}(\rho_{\rm c,def}/\mathrm{g\ cm^{-3}})$ = 9.96, 9.98 and 10.02, respectively.

(c) "046" and "049" stand for $Y_e = 0.46$ and 0.49, respectively, at the center of case (3) models (L_no_mix) and case (2) models (S_ρ_mix). Y_e of case (1) models (Ledoux mix o-burn) is shown as "049" (see (e) below).

(d) "30" and "60" stand for the initial flame at a distance of 30 and 60 km from the center, respectively.

(e) Models with an ending "-LM" represent those of case (1) above, i.e., L_no_mix + mixed region above the oxygen-ignited shell. In these models, "049" stands for $Y_e = 0.49$ in the oxygen-burning mixed shell.

3.3. *Off-Center Runaway with Mixing (Ledoux mix o-burn "LM" Models)*

These models come from the evolution of the ONeMg core using the Ledoux criterion with the off-center convective mixing (see Ledoux mix o-burn in Figure 12). When the off-center oxygen burning is ignited, the generated energy drives the convection from the burning location to the outer part.

To construct the initial models, we first use the Y_e and temperature profiles obtained from Section 2. Then we estimate the convective mixing which produces approximately $Y_e = 0.49$. Within the region of $M_r < M_{r,\rm ign}$, no mixing is assumed and the Y_e profile is directly taken from the stellar evolutionary model. Thus we set the following Y_e distribution as seen in Figure 12. At $M_r < M_{r,\rm ign}$, $Y_e = 0.46$ - 0.47, while at $M_{r,\rm ign} < M_r < 0.14$ $M_\odot$, $Y_e = 0.49$. At $M_r > 0.14$ $M_\odot$ Y_e follows the stellar evolutionary model again.

We do not change the temperature since the matter is extremely degenerate such that the role of temperature is unimportant compared to $Y_{\rm e}$.

In §3.3.1, we run the models with $\rho_{\rm c,def}$ as a parameter to see how the final fate depends on it.

3.3.1. *$\rho_{\rm c,def}$-dependence*

In Figure 13 we plot the central density and central Y_e against time for Models 6-0996-049-30-LM, 6-0998-049-30-LM and 6-1000-049-30-LM in the left and right panels respectively.

There is a time lapse ~ 0.1 s which is the time for the flame to arrive at the center to trigger the early

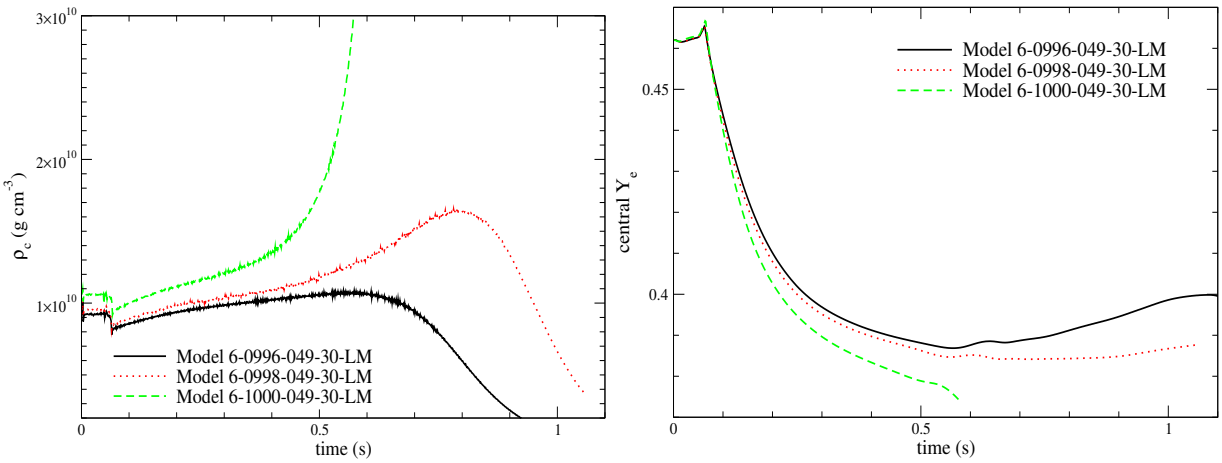

Figure 13. $\rho_{\rm c,def}$-dependence of "Ledoux mix o-burn" models for $\dot{M} = 10^{-6}\ M_\odot\ {\rm yr}^{-1}$. (left panel) The central density evolution of Models 6-0996-049-30-LM (black solid line), 6-0998-049-30-LM (red dotted line) and 6-1000-049-30-LM (green dashed line). The time lapse of ~ 0.1 s is the time for the flame to arrive at the center to trigger the initial expansion. The collapsing model (green dashed line) shows a monotonic increase of the central density after the early expansion, while the other two exploding models show a turning point after which the star expands due to the energy input by oxygen deflagration. (right panel) Similar to the left panel but for the central Y_e.

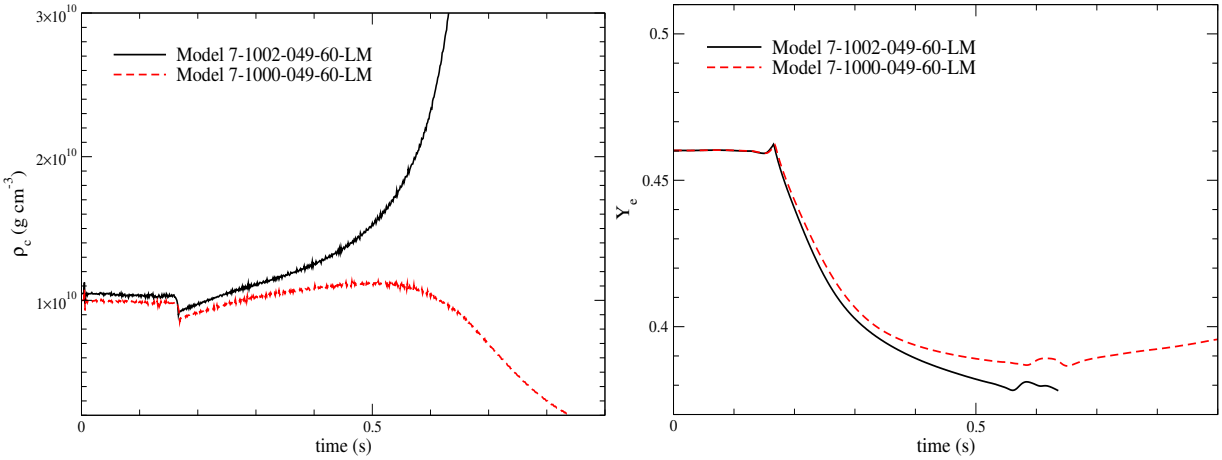

Figure 14. $\rho_{\rm c,def}$-dependence of "Ledoux mix o-burn" models for $\dot{M} = 10^{-7}\ M_\odot\ {\rm yr}^{-1}$. (left panel) The central density evolution of Models 7-1002-049-60-LM (black solid line) and 7-1000-049-60-LM (red dashed line). Similar to Figure 13, the time lapse of ~ 0.2 s is the time for the flame to arrive at the center to trigger the initial expansion. The collapsing model (black solid line) shows a monotonic increase of the central density after the early expansion, while the exploding model (red dashed line) shows a turning point after which the star expands due to the energy input by oxygen deflagration. (right panel) Similar to the left panel but for the central Y_e.

expansion. The model which collapses shows a monotonic increase in the central density after the early expansion. For $\log_{10}(\rho_{\rm c,def}/{\rm g\ cm^{-3}}) \gtrsim 10.00$, the ONeMg core collapses to form a NS. Models which eventually explode show a turning point in the central density evolution. This is the moment when the energy input by the oxygen deflagration dominates the dynamical process in the star. We remark that for the model close to the bifurcation point, i.e., Model 6-0998-049-30, the central density at the turning point is as high as $\log_{10}(\rho_{\rm c}/{\rm g\ cm^{-3}}) = 10.18$.

We also study the hydrodynamical outcomes for the model set with $\dot{M} = 10^{-7}\ M_\odot\ {\rm yr}^{-1}$. In Figure 14 we plot the central density and Y_e evolution for Models 7-1000-046-60-LM and 7-1002-049-60-LM. Compared with the "6"-series, these two models have a farther off-center ignition at 60 km, which requires a longer time (~ 0.2 s) for the flame to reach the center. It thus provides more time for the flame to develop in its size and surface area, which may balance the contraction after electron capture occurs in the center.

When the flame arrives at the center, the heated core again rapidly expands by $\sim 20\%$. Then the rapid electron capture in the NSE ash induces the first contraction. For $\log_{10}(\rho_{\rm c,def}/{\rm g\ cm^{-3}}) = 10.02$, the core continues to collapse. For $\log_{10}(\rho_{\rm c,def}/{\rm g\ cm^{-3}}) = 10.00$, the expansion starts at $t \approx 0.6$ s. The electron capture fails to trigger sufficiently strong contraction before the flame can release the necessary energy to make the star explode.

3.4. *Centered Runaway with Mixing (S_ρ_mix Models)*

When we apply the Schwarzschild criterion, convection can develop in the core before the oxygen ignition. The convective flow transports heat away from the center, which is the first place expected for the nuclear runaway, and uniformly mix the material as seen in Figure 9. To construct the models in Figure 12, we adopt the Y_e profile of S_ρ_mix in Figure 9. Major differences in the initial models from those in §3.3 are the flat Y_e distribution in the core and the centered flame.

We also notice that this scenario is also possible for the Ledoux criterion. As described in Table 3, the exact abundance of ^{12}C and ^{20}Ne depends on the nuclear reaction rate. When we use the updated reaction rate 'jina_reaclib' the higher $X(^{20}{\rm Ne})$ leads to the oxygen ignition at the center. And even with the Ledoux criterion, a convective core driven by the oxygen burning develops from the center afterwards.

3.4.1. $\rho_{\rm c,def}$-*dependence*

As discussed in §2.7, the core continues to contract to a higher $\rho_{\rm c,def}$ until the thermonuclear runaway starts. Since the exact $\rho_{\rm c,def}$ depends on the efficiency of the convective energy transport, we examine how the outcome of the deflagration depends on $\rho_{\rm c,def}$.

In the left panel of Figure 15 we show the central density evolution of two models with $\log_{10}(\rho_{\rm c,def}/{\rm g\ cm^{-3}}) = 9.96$ and 10.00. Both models directly collapse. The minimum $\log_{10}(\rho_{\rm c,def}/{\rm g\ cm^{-3}})$ for the ONeMg core to collapse is 9.96, which is even lower than 10.00 of the MESA model with the Schwarzschild criterion (S_ρ_mix). We also plot the central Y_e evolution in the right panel, which smoothly decreases without any bump.

The "7"-series models with different $\rho_{\rm c,def}$ (7-0997-049-00 and 7-1000-049-00) are plotted in the Figure 16. The high Y_e (=0.49) again allows the ONeMg core to collapse at $\log_{10}(\rho_{\rm c,def}/{\rm g\ cm^{-3}}) = 9.97$, which is lower than $\log_{10}(\rho_{\rm c,ign}/{\rm g\ cm^{-3}})$ =10.00 of stellar evolutionary model (S_ρ_mix).

3.4.2. $r_{\rm ign}$-*dependence*

For models with the central oxygen ignition, the center is the most likely position for the oxygen deflagration to start because the convection developed from the center will smooth out any temperature inversion in the star. However, when the convective flow is strong, the potential fluid parcel which will undergo the nuclear runaway may be carried away by the flow before the runaway is triggered. As a result, an off-center flame can be developed. Therefore, the exact $r_{\rm ign}$ could be non-zero and depends on the detailed characteristic of the convective flow. Here, we study the uncertainties in this parameter.

We simulate the propagation of the oxygen deflagration with different initial flame structures. In Figure 17 we compare the evolution of Models 6-0996-049-30, 6-0996-049-00, 6-1000-049-30 and 6-1000-049-00. They are two sets of models with the centered (-00) and off-center flame (-30). The two $\rho_{\rm c,def}$ correspond to $\rho_{\rm c,ign}$, i.e., the lowest cases of $\rho_{\rm c,def}$ obtained from the Ledoux (0996) and Schwarzschild (1000) criteria, respectively.

Figure 17 shows that all four models directly collapse. As discussed in the previous section, the position of the initial flame affects the early evolution of the central density. Models with a centered flame show a rapid drop in ρ_c at the beginning, but then the following electron capture makes the core contract again and ρ_c increase until the simulations end. Models with an off-centered flame show no change in ρ_c until the flame arrives at the center at $t \approx 0.08$ s. After the rapid drop by $\sim 10\%$, ρ_c increases again until the end of simulations. Therefore, for models with $r_{\rm ign} = 30$ km, the position of the initial flame is less important for the final fate of the ONeMg core.

In the right panel of Figure 17 we plot the central density evolution for Models 7-0997-049-60, 7-0997-049-00, 7-1000-049-60 and 7-1000-049-00. The two models with a higher $\rho_{\rm c,def}$ collapse. However, different from the models with $r_{\rm ign} = 30$ km, the lower $\rho_{\rm c,def}$ model with a centered flame collapses while that with an off-center flame ($r_{\rm ign} = 60$ km) explodes.

3.5. *Off-center Runaway without Mixing (L_no_mix Models)*

Here we examine the model developed from the model L_no_mix. This is another limiting case in our model survey, where we assume no convective mixing appears despite that the oxygen burning creates a convectively unstable region even with the Ledoux criterion. As a result, the oxygen-ignited site becomes the site for the nuclear runaway.

3.5.1. $\rho_{\rm c,def}$-*dependence*

We examine the dependence of the evolution of the ONeMg core on the initial central density $\rho_{\rm c,def}$. Even neglecting the convective energy transport, the timescale of the temperature rise due to early phase of

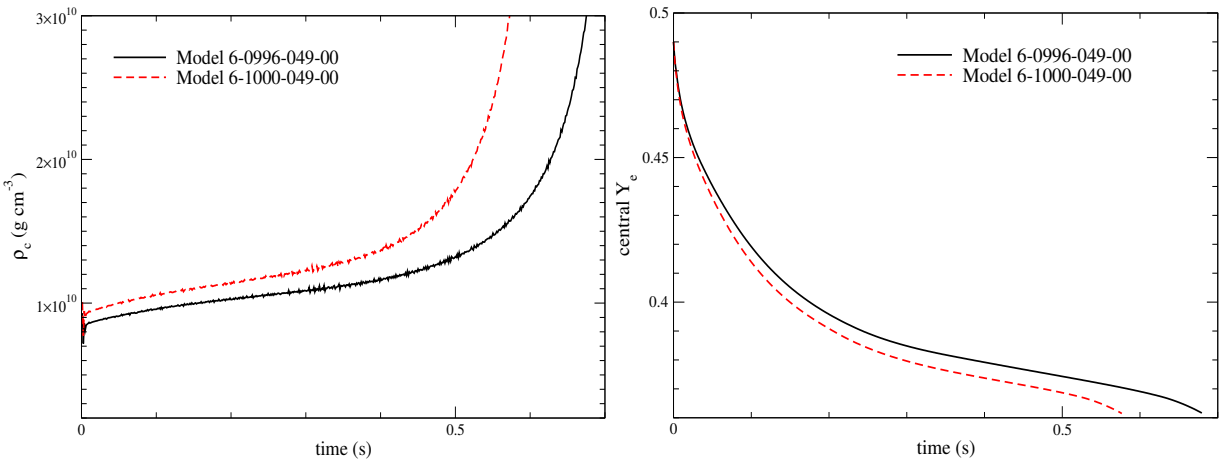

Figure 15. $\rho_{\rm c,def}$-dependence of "S_ρ_mix" models for $\dot{M} = 10^{-6}\ M_\odot\ {\rm yr}^{-1}$. (left panel) The central density evolution of Models 6-0996-049-00 (black solid line) and 6-1000-049-00 (red dashed line). Model 6-1000-049-00 corresponds to the stellar evolutionary model S_ρ_mix. (right panel) Similar to the left panel but for the central $Y_{\rm e}$.

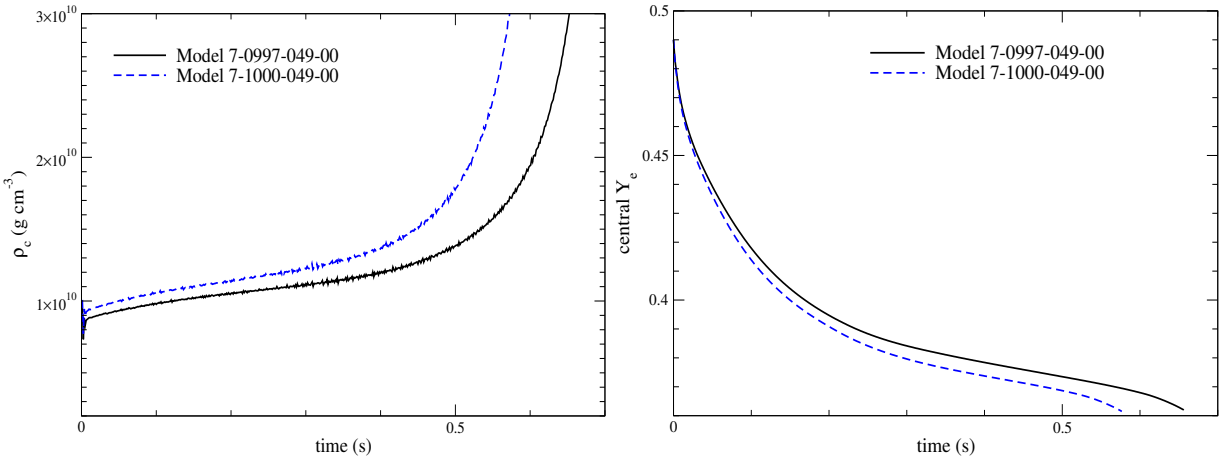

Figure 16. $\rho_{\rm c,def}$-dependence of "S_ρ_mix" models for $\dot{M} = 10^{-7}\ M_\odot\ {\rm yr}^{-1}$. (left panel) The central density evolution of Models 7-0997-049-00 (black solid line) and 7-1000-049-00 (blue dashed line). Model 7-1000-049-00 corresponds to the stellar evolutionary model S_ρ_mix. (right panel) Similar to the left panel but for the central $Y_{\rm e}$.

the oxygen burning is still longer than the timescale of core contraction due to electron capture. Therefore $\rho_{\rm c,def}$ can become somewhat higher than $\rho_{\rm c,ign}$.

In the left panel of Figure 18 we plot the central density evolution for 5 models from 6-0996-046-30 to 6-1020-046-30, where the flame position and the temperature and Y_e profiles against M_r are the same. Y_e at the center is as low as 0.46. Model 6-0996-046-30 corresponds to the model L_no_mix without contraction after the oxygen ignition, i.e., $\rho_{\rm c,def} = \rho_{\rm c,ign}$. The central density remains unchanged again for the first 0.1 s. Then, the central density shows a sudden drop as the burnt matter in the center expands. After that, the central density increases again. For models with a higher $\rho_{\rm c,def}$, the contraction is faster. Models with $\log_{10}(\rho_{\rm c,def}/{\rm g\ cm^{-3}}) \geq 10.05$ collapse into NSs.

In the right panel of Figure 18, we show the corresponding central Y_e evolution. Before the flame reaches the center, Y_e remains unchanged. However, once the material is burnt into NSE, Y_e quickly drops from its original value to $\sim 0.38 - 0.40$ within 0.1 - 0.2 s. For a higher $\rho_{\rm c,def}$, the electron capture takes place faster. For models which explode, the central Y_e increases mildly when the central matter is mixed with the outer high Y_e material, until it reaches an asymptotic value.

In the left panel of Figure 19 we plot the central density evolution for 4 models from 7-0997-046-60 to 7-1010-046-60. Model 7-0997-046-60 corresponds to the model L_no_mix without contraction after the oxygen ignition, i.e., $\rho_{\rm c,def} = \rho_{\rm c,ign}$. For models with $\log_{10}(\rho_{\rm c,def}/{\rm g\ cm^{-3}}) \geq 10.05$, they collapse into NSs. It takes a longer time of ~ 0.15 s for the flame to reach

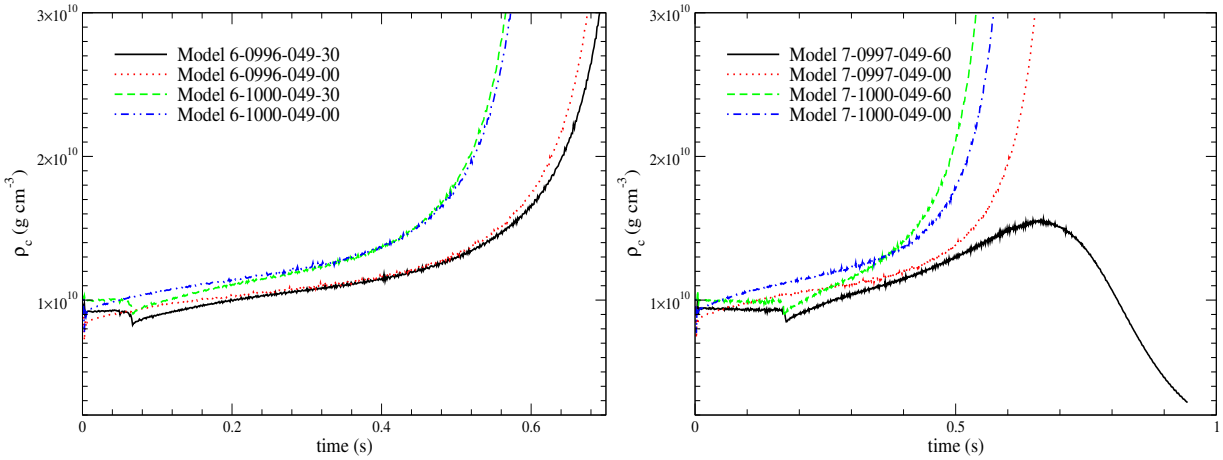

Figure 17. $\rho_{\rm c,def}$ and $r_{\rm ign}$-dependence of "S_ρ_mix" models for $\dot{M} = 10^{-6}$ and 10^{-7} $M_\odot$ yr^{-1}. (left panel) The central density evolution of Models 6-0996-049-30 (black solid line), 6-0996-049-00 (red dotted line), 6-1000-049-30 (green dashed line), 6-1000-049-00 (blue dot-dashed line). (right panel) Similar to the left panel but for the Models 7-0997-049-60 (black solid line), 7-0997-049-00 (red dotted line), 7-1000-049-60 (green dashed line), 7-1000-049-00 (blue dot-dashed line).

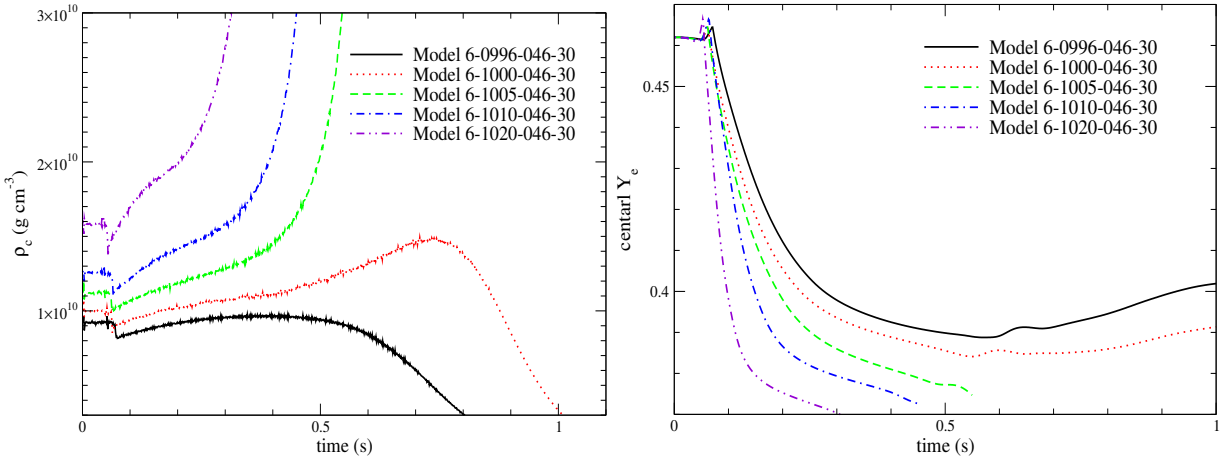

Figure 18. $\rho_{\rm c,def}$-dependence of "L_no_mix" models for $\dot{M} = 10^{-6}$ $M_\odot$ yr^{-1}. (left panel) The central density evolution of Models 6-0996-046-30 (black solid line), 6-1000-046-30 (red dotted line), 6-1005-046-30 (green dashed line), 6-1010-046-30 (blue dot-dashed line), 6-1020-046-30 (purple dot-dot-dashed line). Notice that Model 6-0996-046-30 corresponds to the MESA model L_no_mix without contraction after the oxygen ignition, i.e., $\rho_{\rm c,def} = \rho_{\rm c,ign}$. (right panel) Similar to the left panel but for the central $Y_{\rm e}$.

the center. Then the early expansion and the subsequent contraction due to electron capture take place. The contraction is weaker than the case for $\dot{M} = 10^{-6}$ $M_\odot$ yr^{-1} because the flame has more time to propagation before central electron capture induces the rapid contraction. A maximum $\log_{10}(\rho_{\rm c}/{\rm g\ cm^{-3}})$ of ~ 10.00 is found for the turning point of the exploding models. At $t \sim 0.5$ s, the core begins its expansion.

In the right panel, we plot the corresponding central Y_e evolution. The qualitative feature of the Y_e evolution is similar to the "6"-series models. Models which explode reach a minimum Y_e of ~ 0.39. For those which collapse, Y_e continues to drop before the simulations stop. From the two set of models, it suffices to see that, despite the initial configurations are different, the models still show a strong sensitivity on $\rho_{\rm c,def}$. In particular, the exact value of $\log_{10}(\rho_{\rm c,def}/{\rm g\ cm^{-3}})$ is important because the minor change from 10.0 to 10.05 is sufficient to change the core from explosion to collapse.

3.5.2. $r_{\rm ign}$-*dependence*

Depending on the nuclear reaction network, as discussed in §2.6.3, the initial runaway position can change from off-center ($\sim 30 - 60$ km) to the center. Here we briefly examine how the models vary by considering the different possible position of the initial flame.

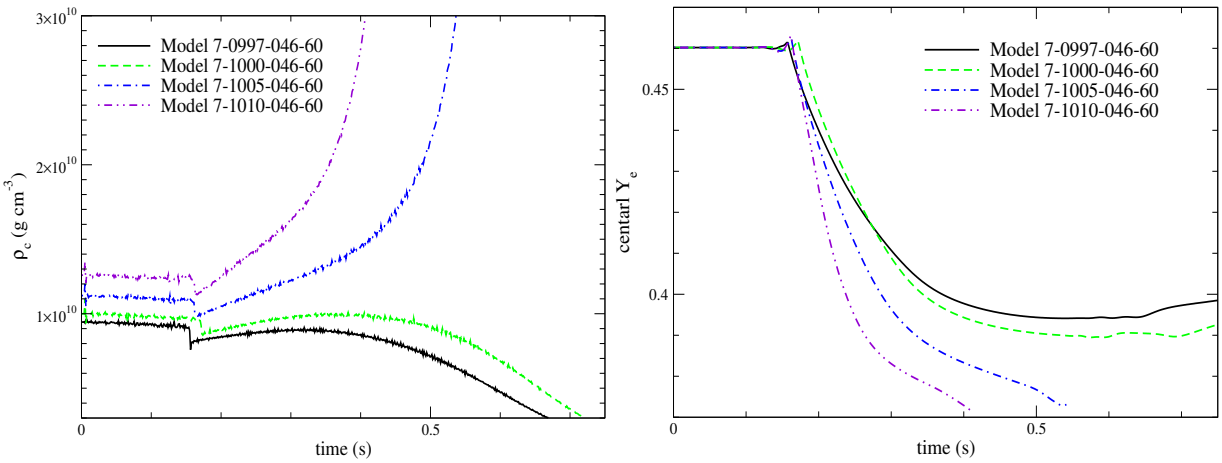

Figure 19. $\rho_{\rm c,def}$-dependence of "L_no_mix" models for $\dot{M} = 10^{-7}\ M_\odot\ {\rm yr}^{-1}$. (left panel) The central density evolution of Models 7-0997-046-60 (black solid line), 7-1000-046-60 (green dashed line), 7-1005-046-60 (blue dot-dashed line), 7-1010-046-60 (purple dot-dot-dashed line). Notice that Model 7-0997-046-60 corresponds to the oxygen-ignition model L_no_mix without contraction after the oxygen ignition, i.e., $\rho_{\rm c,def} = \rho_{\rm c,ign}$. (right panel) Similar to the left panel but for the central $Y_{\rm e}$.

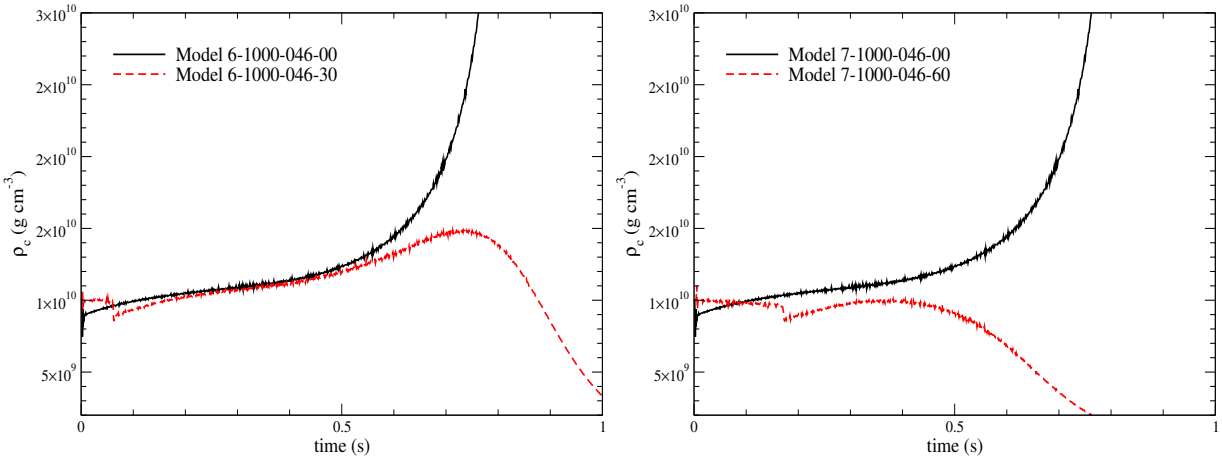

Figure 20. $r_{\rm ign}$-dependence of "L_no_mix" models for $\dot{M} = 10^{-6}$ and $10^{-7}\ M_\odot\ {\rm yr}^{-1}$. (left panel) The central density evolution of Models 6-1000-046-00 (black solid line) and 6-1000-046-30 (red dotted line). (right panel) Similar to the left panel but for the Models 7-1000-046-00 (black solid line) and 7-1000-046-60 (red dotted line).

In Figure 20 we plot the central density evolution for Models 6-1000-046-30 and 6-1000-046-00 in the left panel and Models 7-1000-046-60 and 7-1000-046-00 in the right panel. Here we see the contrasting final fates when the flame starts at the center or off-center. For the centered flame in both cases, a direct collapse of ONeMg core is observed. On the other hand, an off-center flame leads to explosion. Furthermore, in the exploding case, owing to the high initial central density, during the contraction phase the central density can reach as high as $\log_{10}(\rho_{\rm c}/{\rm g\ cm^{-3}}) \sim 10.18$. Such a high central density allows Y_e to reach as low as ~ 0.38. The low Y_e allows formation of extremely neutron-rich isotopes, which may provide characteristic abundances if they are later ejected from the core during explosion.

3.6. *Flame Structure*

In Figure 21 we plot the temperature color map for the collapsing (exploding) model 6-1000-046-00 (6-1000-046-30) at time ~ 0.6 s (~ 1.1 s) after the nuclear runaway has started. The other collapsing or exploding models share the similar properties for the flame structure.

In the collapsing model, the continuing contraction of matter prevents the burnt matter from reaching low density regions. The burnt matter is confined within the radius of ~ 200 km. Outside the flame, most matter remains unperturbed with a low temperature below 10^9 K. The flame appears to be spherical to a good approximation and the central region has in general a low temperature ($\sim 8 \times 10^9$ K). At higher densities, the growth of hydrodynamical instabilities tends to be suppressed be-

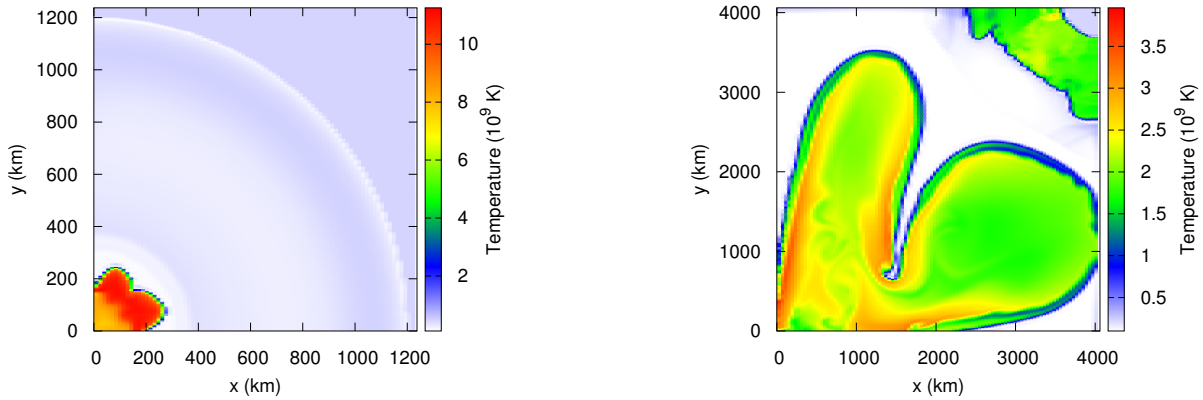

Figure 21. (left panel) The temperature color map of the collapsing model 6-1000-046-00 at the end of simulation (~ 0.6 s) where the central density reaches $10^{10.5}$ g cm^{-3}. (right panel) Similar to the left panel but for the exploding model 6-1000-046-30 at ~ 1.1 s after the nuclear runaway starts. Here the central density is $\sim 10^{9.5}$ g cm^{-3}.

cause the nuclear energy release relative to the internal energy is small.

For the exploding model, the structure of the oxygen deflagration is similar to the carbon deflagration (Leung & Nomoto 2018). The flame is much more extended to a size of ~ 3500 km. One major difference between the oxygen deflagration and carbon deflagration is that the asphericity and hydrodynamical instabilities tend to be suppressed. This is because the nuclear energy release relative to the internal energy is smaller and the effect of electron capture is larger, which leads to the smaller buoyancy force in the oxygen flame than carbon.

3.7. *Summary of Parameter Dependence*

In §3.3-3.5, we have performed the hydrodynamical simulations by adopting the three Y_e distributions at the oxygen ignition: (1) Ledoux mix o-burn (§3.3), (2) S_ρ_mix (§3.4), and (3) L_no_mix (§3.5). Such differences stem from the different treatment of convection. Development of the convection after the oxygen ignition controls the further evolution and determines $\rho_{\rm c,def}$ and the flame location ($r_{\rm ign}$) at the initiation of the oxygen deflagration. In Figure 22 we summarize the dependence of $\rho_{\rm cr}$ (the critical density for explosion-collapse bifurcation) on the physical assumptions, complementary to Table 4. Because of the numerical difficulty to follow the evolution after the oxygen ignition, we have treated $\rho_{\rm c,def}$ and $r_{\rm ign}$ as parameters.

The outcomes of our 2D hydrodynamical simulations depend on the above parameters are summarized in Figures 23 and 24 for $\dot{M} = 10^{-6}\ M_\odot$ yr^{-1} and $10^{-7}\ M_\odot$ yr^{-1}, respectively. Here, the final fate of the ONeMg core is designated as either C (collapse) or E (explosion).

In the abscissa, 3 cases of the initial Y_e distributions are shown as $Y_e = 0.46$ for case (3), $Y_e = 0.49$ for case (2), and case (1) (-LM) in between. In the ordinate, $\rho_{\rm c,def}$ is shown.

For case (1) (-LM), if $\log_{10}(\rho_{\rm c,def}/{\rm g\ cm^{-3}}) \geq 9.99$ and 10.02, the final fate is the collapse for $r_{\rm ign} =$ 30 km and 60 km, respectively. On the contrary, if $\log_{10}(\rho_{\rm c,def}/{\rm g\ cm^{-3}}) \leq 9.98$ and 10.00, respectively, the final fate would be the explosion. In other words, the critical density for the collapse to occur is $\log_{10}(\rho_{\rm cr}/{\rm g\ cm^{-3}}) \approx 9.985$ and 10.01 for $r_{\rm ign} = 30$ km and 60 km, respectively.

For case (2) ($Y_e = 0.49$) with the Schwarzshild criterion, most models collapse, and even the critical density is smaller than the central density at the oxygen ignition, i.e., $\log_{10}(\rho_{\rm cr}/{\rm g\ cm^{-3}}) < \log_{10}(\rho_{\rm c,ign}/{\rm g\ cm^{-3}}) \approx 9.97$.

For case (3) with no mixing, $\log_{10}(\rho_{\rm cr}/{\rm g\ cm^{-3}}) \simeq 10.05$. If $\log_{10}(\rho_{\rm c,def}/{\rm g\ cm^{-3}}) \gtrsim 10.15$ as we estimated for the evolution after the oxygen ignition (§2.7), $\rho_{\rm cr} > \rho_{\rm c,def}$, i.e., the collapse is the most likely outcome.

3.8. *Astrophysical Significance*

In the previous sections, we have shown that the collapse is the more likely outcome of an ECSN. This collapse would be similar to the ONeMg core of the 8.8 $M_\odot$ star (Nomoto 1984; Kitaura et al. 2006; Wanajo et al. 2011). If this similarity is the case, the neutrino heating mechanism works to induce a low-energy explosion thanks to the steep density gradient in the outermost layers. The very extended H-He super-AGB envelope would be easily ejected and a NS would be formed. If the mass ejection from the core is negligible, the baryonic mass of the NS is in the range of $1.357 - 1.361\ M_\odot$ (Table 2). If the ejected mass is $1.14 - 1.39 \times 10^{-2}\ M_\odot$ (like in Kitaura et al. 2006; Wanajo et al. 2011), then

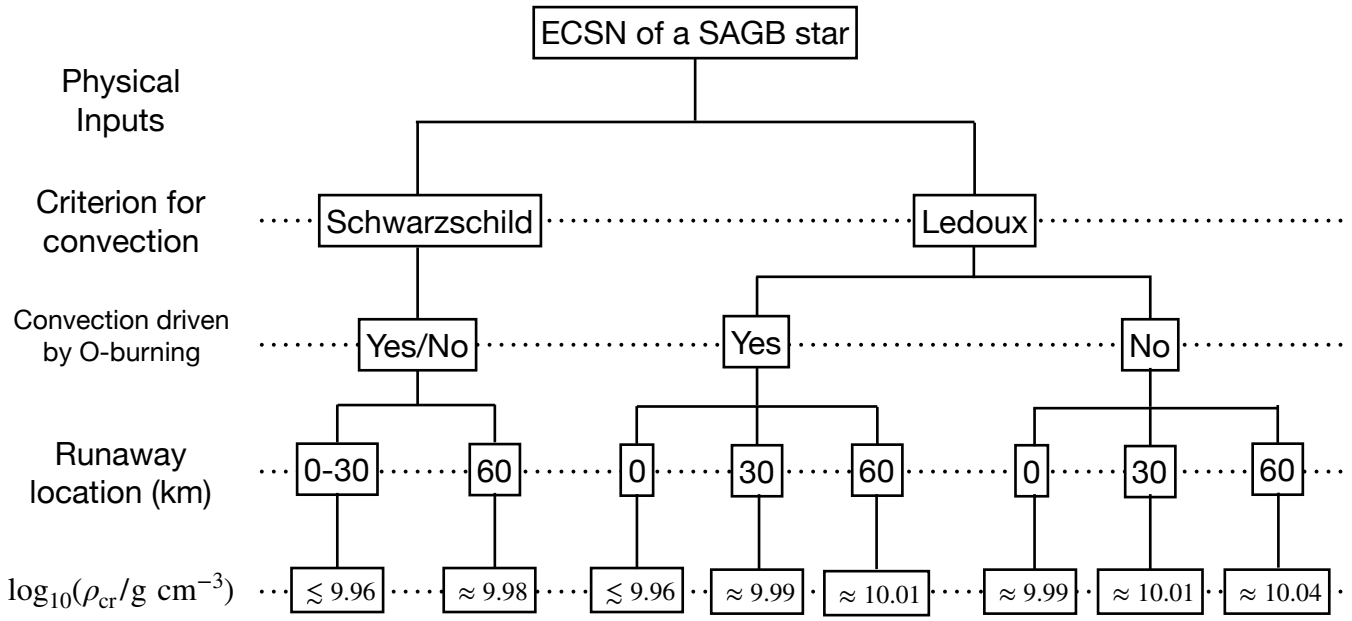

Figure 22. Summary of the critical density for the explosion-collapse bifurcation, $\rho_{\rm cr}$, from the 2D hydrodynamical simulations with different physical assumptions (see also Table 4 and Figures 23 and 24). The physical assumptions include the criterion for the convective stability (Schwarzschild or Ledoux), the convection driven by the oxygen burning, and the thermonuclear runaway location. Here the runaway location depends on the accretion rate (§2.6.2), ^{12}C$(\alpha,\gamma)^{16}$O reaction rate (§2.6.3), and the convective flow in the flame (§3.4.2).

it would be $1.343 - 1.350\ M_\odot$. This is smaller than $\sim 1.36\ M_\odot$ of the $8.8\ M_\odot$ model (Kitaura et al. 2006), because of the lower Y_e in the ONeMg core.

The super-AGB progenitors are different from more massive stars, undergoing a large amount of mass loss. Such mass loss would lead to a small mass of the H-He envelope and a large amount of circumstellar material (CSM), possibly with lots of carbon dust. The supernova properties depend on the masses of the H-He envelope and CSM, and the optical light curve could be similar to the Fast-evolving Blue Optical Transient (Tolstov et al. 2019) or the Crab supernova (Nomoto et al. 1982; Tominaga et al. 2013; Moriya et al. 2014). It might be Type II-L like supernovae because of the low envelope mass. If CSM is very dusty, it would be bright in infrared, like the eSPecially Red Intermediate-luminosity Transient Events (Kasliwal et al. 2017). The above properties are somewhat different from typical Type II-P Fe-core-collapse supernovae.

On the other hand, if the ONeMg core (partially) explodes as a result of the oxygen deflagration, it could be a weak thermonuclear explosion within a H-He envelope, leaving a WD behind. The oxygen deflagration cannot burn all materials in the star, and it results in a partial disruption of the ONeMg core (Jones et al. 2016). The turbulent mixing by the flame allows the ejecta to consist of both Fe-peak elements and the ONe-rich fuel. Ejecta can be rich in neutron-rich isotopes, e.g., ^{48}Ca, ^{50}Ti, ^{54}Cr, and ^{60}Fe (Jones et al. 2019). The light curve is dimmer than a normal Type II supernova, due to a smaller mass of ^{56}Ni synthesized. It could be called as a Type I.5ax supernova (like Type Iax).

4. SUMMARY

We have calculated the evolution of the $8.4\ M_\odot$ star from the main sequence until the oxygen ignition in the degenerate ONeMg core, where the nuclear energy generation rate exceeds the thermal neutrino loss rate and a convective region develops. We have applied the latest weak rates (Suzuki et al. 2019), including the second forbidden transition for the electron capture on ^{20}Ne (Kirsebom et al. 2018). The electron-degenerate ONeMg core evolves through complicated processes of the mass accretion, election capture heating, URCA cooling, and the Y_e change due to weak interactions. The convective and semiconvective regions are formed. Because of uncertainties in the semiconvective mixing, we have applied both the Ledoux and Schwarzshild cri-

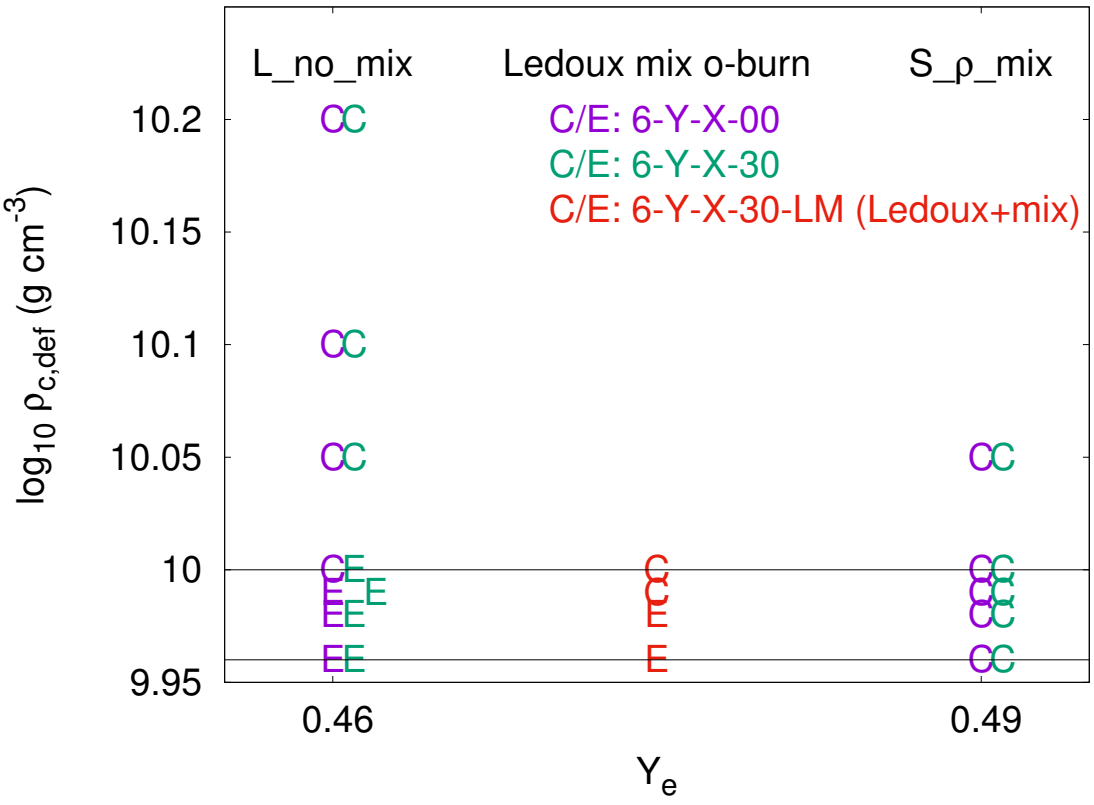

Figure 23. The explosion-collapse bifurcation diagram as a function of $\rho_{\rm c,def}$ and the initial Y_e distribution. $Y_e = 0.46$ and 0.49 are the central Y_e of case (3) modesl (L_no_mix) and case (2) models (S_ρ_mix), respectively. Between these cases, case (1) models (Ledoux mix o-burn) are shown. The data is taken from models with $\dot{M} = 10^{-6}\ M_\odot\ {\rm yr}^{-1}$. "E" and "C" stand for "Explosion" and "Collapse", respectively.

teria for the convective stability. Our findings of the ONeMg core evolution are summarized as follows.

(1) If we apply the Ledoux criterion and assume no mixing, we have found the following evolution. The second forbidden transition is so slow that it does not ignite oxygen burning at the related threshold density, but decreases the central Y_e to ~ 0.46 during the core contraction. The oxygen ignition takes place when the central density reaches $\log_{10}(\rho_{\rm c,ign}/{\rm g\ cm^{-3}}) = 9.96 - 9.97$. The location of the oxygen ignition, i.e., center or off-center ($r_{\rm ign} \sim 30 - 60$ km), depends on the $^{12}{\rm C}(\alpha,\gamma)^{16}{\rm O}$ reaction rate because it affects the ^{20}Ne mass fraction by a few percent in the ONeMg core.

(2) If we apply the Schwarzshild criterion, the convective core heated up by electron capture on ^{20}Ne can grow to half of the mass of the ONeMg core. The oxygen ignition takes place at the center. The convective energy transport delays the oxygen ignition until $\log_{10}(\rho_{\rm c,ign}/{\rm g\ cm^{-3}}) \sim 10.0$ is reached, and the convective mixing makes Y_e in the convective region as high as 0.49.

(3) Even with the Ledoux criterion, the oxygen ignition (at the center or off-center) creates the convectively unstable region and the convective mixing forms an extended region with $Y_e \sim 0.49$ above the oxygen ignited shell. The convective energy transport would slow down the temperature increase, and so the thermonuclear runaway to form a deflagration wave is estimated to occur when the central density $\log_{10}(\rho_{\rm c,def}/{\rm g\ cm^{-3}})$ exceeds 10.10. (This estimate is consistent with the result by Takahashi et al. (2019), who obtained $\log_{10}(\rho_{\rm c,def}/{\rm g\ cm^{-3}}) \approx 10.2$ with a semi-convection coefficient of Spruit (1992).)

Then, to examine the final fate of the ONeMg core, we have performed 2D hydrodynamical simulations of the propagation of the oxygen deflagration wave for the three cases of the Y_e distribution, three locations of the oxygen ignition, and various $\rho_{\rm c,def}$. We have found that the deflagration starting from $\log_{10}(\rho_{\rm c,def}/{\rm g\ cm^{-3}}) > 10.01 (< 10.01)$ leads to a collapse (a thermonuclear explosion). Since our estimate of $\rho_{\rm c,def}$ well exceeds this critical value, the ONeMg core is likely to collapse ir-

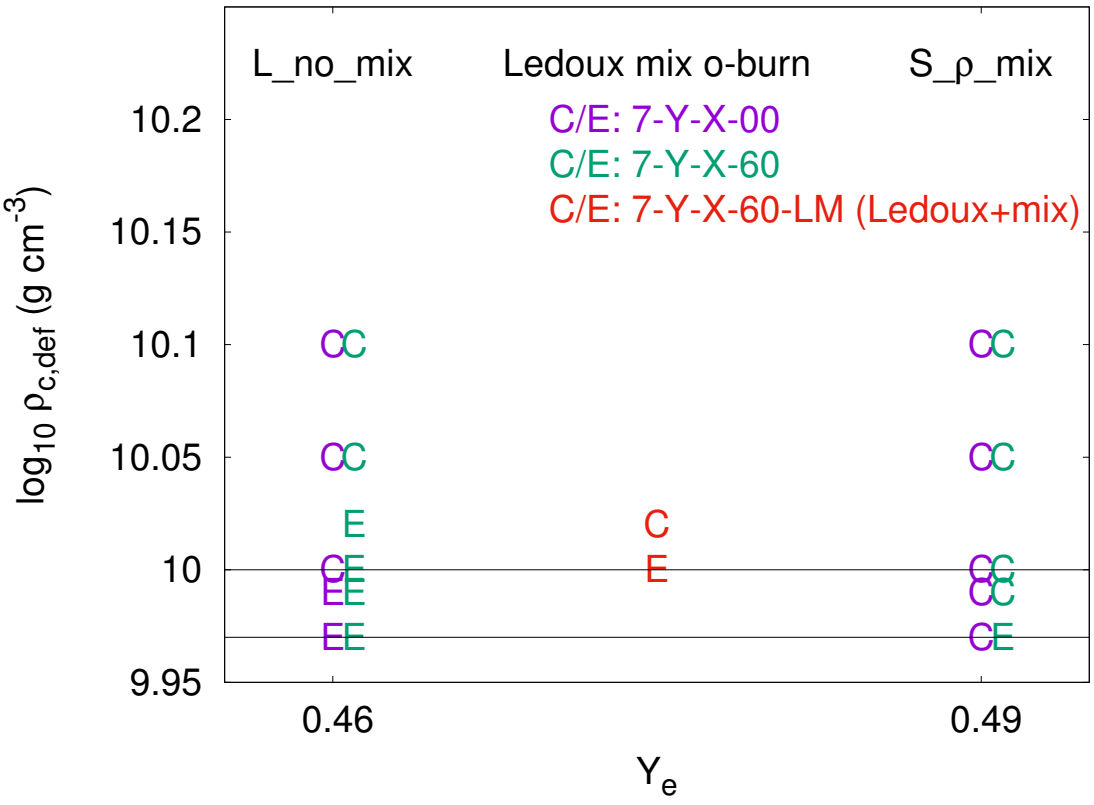

Figure 24. Similar to Figure 23 but the data are taken from models with $\dot{M} = 10^{-7}\ M_\odot\ \mathrm{yr}^{-1}$.

respective of the central Y_e and ignition position (Figures 23 and 24).

Our work has shown that the degenerate ONeMg core evolved in a SAGB star can collapse to form a relatively low mass NS. However, future work needs to confirm whether such a high $\rho_{\mathrm{c,def}}$ is reached by calculating the evolution of the core with semiconvection and with the full convection from the oxygen ignition through the initiation of the deflagration by improving the stellar evolution modeling.

5. ACKNOWLEDGMENT

The results in this paper have been presented at the Lorentz Center workshop on "Electron-Capture-Initiated Stellar Collapse". We would like to thank the Lorentz Center and the workshop participants for stimulated discussion. Near the end of the workshop, Kirsebom et al. (2019) was submitted. We will make comparisons in a separate paper. This work was supported by World Premier International Research Center Initiative (WPI), MEXT, Japan and JSPS KAKENHI Grant Numbers JP17K05382, JP19K03855, and a grant from the Research Grant Council of Hong Kong (Project 14300317). We acknowledge the support of the CUHK Central High Performance Computing Cluster, on which the stellar evolution simulation in this work has been performed. We thank F.-X. Timmes for the open-source subroutines of the helmholtz equation of state and torch nuclear reaction network. We also thank MESA developers for making their code open-source.

Software: MESA (Paxton et al. 2011, 2013, 2015, 2018, 2019); NuGridPy (available from https://nugrid.github.io/NuGridPy/)

REFERENCES

An, Z.-D., Ma, Y.-G., Fan, G.-T., et al. 2016, ApJ, 817, L5

Barth, T. J., & Deconinck, H. 1999, Lecture Notes in Computational Science and Engineering 9: High-Order Methods for Computational Physics (Springer)

Bloecker, T. 1995, A&A, 299, 755
Brown, B. A., & Richter, W. A. 2006, PhRvC, 74, 034315
Calder, A. C., Townsley, D. M., Seitenzahl, I. R., et al. 2007, ApJ, 656, 313
Caughlan, G. R., & Fowler, W. A. 1988, Atomic Data and Nuclear Data Tables, 40, 283
Clement, M. J. 1993, ApJ, 406, 651
Cyburt, R. H., Amthor, A. M., Ferguson, R., et al. 2010, ApJS, 189, 240
Denissenkov, P. A., Truran, J. W., Herwig, F., et al. 2015, MNRAS, 447, 2696
Doherty, C. L., Gil-Pons, P., Siess, L., & Lattanzio, J. C. 2017, Publications of the Astronomical Society of Australia, 34, e056
Doherty, C. L., Gil-Pons, P., Siess, L., Lattanzio, J. C., & Lau, H. H. B. 2015, MNRAS, 446, 2599
Fantina, A. F., Khan, E., Colò, G., Paar, N., & Vretenar, D. 2012, Phys. Rev. C, 86, 035805
Farmer, R., Fields, C. E., & Timmes, F. X. 2015, ApJ, 807, 184
Fryer, C., Benz, W., Herant, M., & Colgate, S. A. 1999, ApJ, 516, 892
Fuller, G. M., Fowler, W. A., & Newman, M. J. 1980, ApJS, 42, 447
—. 1985, ApJ, 293, 1
Gutiérrez, J., Canal, R., & García-Berro, E. 2005, A&A, 435, 231
Höfner, S., & Olofsson, H. 2018, A&A Rv, 26, 1
Iben, I., J. 1978, ApJ, 226, 996
Jones, S., Röpke, F. K., Pakmor, R., et al. 2016, A&A, 593, A72
Jones, S., Hirschi, R., Nomoto, K., et al. 2013, ApJ, 772, 150
Jones, S., Röpke, F. K., Fryer, C., et al. 2019, A&A, 622, A74
Juodagalvis, A., Langanke, K., Hix, W. R., Martínez-Pinedo, G., & Sampaio, J. M. 2010, NuPhA, 848, 454
Kasliwal, M. M., Bally, J., Masci, F., et al. 2017, VizieR Online Data Catalog, J/ApJ/839/88
Kippenhahn, R., Weigert, A., & Weiss, A. 2012, Stellar Structure and Evolution
Kirsebom, O. S., Hukkanen, M., Kankainen, A., et al. 2018, arXiv e-prints, arXiv:1805.08149
Kirsebom, O. S., Jones, S., Strömberg, D. F., et al. 2019, arXiv e-prints, arXiv:1905.09407
Kitaura, F. S., Janka, H.-T., & Hillebrandt, W. 2006, A&A, 450, 345
Kunz, R., Fey, M., Jaeger, M., et al. 2002, ApJ, 567, 643
Langanke, K., & Martínez-Pinedo, G. 2000, Nuclear Physics A, 673, 481
Langanke, K., & Martínez-Pinedo, G. 2001, Atomic Data and Nuclear Data Tables, 79, 1
Leung, S.-C., Chu, M.-C., & Lin, L.-M. 2015a, MNRAS, 454, 1238
—. 2015b, ApJ, 812, 110
Leung, S.-C., & Nomoto, K. 2018, ApJ, 861, 143
—. 2019a, Publications of the Astronomical Society of Australia, 36, e006
—. 2019b, ApJ submitted, arXiv:1901.10007
Leung, S.-C., Nomoto, K., & Suzuki, T. 2019, ApJ submitted, arXiv:1901.11438
Leung, S.-C., Shuai, Z., Chu, M.-C., & Lin, L.-M. 2019, In Preparations
Martínez-Pinedo, G., Lam, Y. H., Langanke, K., Zegers, R. G. T., & Sullivan, C. 2014, PhRvC, 89, 045806
Martínez-Pinedo, G., & Langanke, K. 1999, PhRvL, 83, 4502
Miyaji, S., & Nomoto, K. 1987, ApJ, 318, 307
Miyaji, S., Nomoto, K., Yokoi, K., & Sugimoto, D. 1980, Publications of the Astronomical Society of Japan, 32, 303
Moriya, T. J., Tominaga, N., Langer, N., et al. 2014, A&A, 569, A57
Nabi, J.-U., & Klapdor-Kleingrothaus, H. V. 1999, Atomic Data and Nuclear Data Tables, 71, 149
Niemeyer, J. C., & Hillebrandt, W. 1995, ApJ, 452, 769
Nomoto, K. 1984, ApJ, 277, 791
—. 1987, ApJ, 322, 206
Nomoto, K., Kobayashi, C., & Tominaga, N. 2013, ARA&A, 51, 457
Nomoto, K., & Kondo, Y. 1991, ApJ, 367, L19
Nomoto, K., & Leung, S.-C. 2017a, Handbook of Supernovae, eds. Alsabti, A.W. & Murdin, P. (Springer), 2017, Vol. 1, p. 483
—. 2017b, Handbook of Supernovae, eds. Alsabti, A.W. & Murdin, P. (Springer), 2017, Vol. 2, p. 1275
Nomoto, K., Miyaji, S., Sugimoto, D., & Yokoi, K. 1979, in IAU Colloq. 53: White Dwarfs and Variable Degenerate Stars, ed. H. M. van Horn, V. Weidemann, & M. P. Savedoff, 56
Nomoto, K., Sparks, W. M., Fesen, R. A., et al. 1982, Nature, 299, 803
O'Connell, J. S., Donnelly, T. W., & Walecka, J. D. 1972, PhRvC, 6, 719
Oda, T., Hino, M., Muto, K., Takahara, M., & Sato, K. 1994a, Atomic Data and Nuclear Data Tables, 56, 231
—. 1994b, Atomic Data and Nuclear Data Tables, 56, 231

Paar, N., Colò, G., Khan, E., & Vretenar, D. 2009, Phys. Rev. C, 80, 055801
Paxton, B., Bildsten, L., Dotter, A., et al. 2011, ApJS, 192, 3
Paxton, B., Cantiello, M., Arras, P., et al. 2013, ApJS, 208, 4
Paxton, B., Marchant, P., Schwab, J., et al. 2015, ApJS, 220, 15
Paxton, B., Schwab, J., Bauer, E. B., et al. 2018, ApJS, 234, 34
Paxton, B., Smolec, R., Gautschy, A., et al. 2019, arXiv e-prints, arXiv:1903.01426
Pocheau, A. 1994, PhRvE, 49, 1109
Radice, D., Burrows, A., Vartanyan, D., Skinner, M. A., & Dolence, J. C. 2017, ApJ, 850, 43
Reimers, D. 1975, Memoires of the Societe Royale des Sciences de Liege, 8, 369
Reinecke, M., Hillebrandt, W., & Niemeyer, J. C. 1999a, A&A, 347, 739
—. 2002, A&A, 386, 936
Reinecke, M., Hillebrandt, W., Niemeyer, J. C., Klein, R., & Gröbl, A. 1999b, A&A, 347, 724
Richter, W. A., Mkhize, S., & Brown, B. A. 2008, PhRvC, 78, 064302
Schmidt, W., Niemeyer, J. C., Hillebrandt, W., & Röpke, F. K. 2006, A&A, 450, 283
Schwab, J., Bildsten, L., & Quataert, E. 2017a, MNRAS, 472, 3390
Schwab, J., Martínez-Rodríguez, H., Piro, A. L., & Badenes, C. 2017b, ApJ, 851, 105
Schwab, J., Quataert, E., & Bildsten, L. 2015, MNRAS, 453, 1910
Schwab, J., & Rocha, K. A. 2019, ApJ, 872, 131
Seitenzahl, I. R., Townsley, D. M., Peng, F., & Truran, J. W. 2009, Atomic Data and Nuclear Data Tables, 95, 96
Spruit, H. C. 1992, A&A, 253, 131
—. 2013, A&A, 552, A76
Sussman, M., Smereka, P., & Osher, S. 1994, JCP, 114, 146
Suzuki, T., Toki, H., & Nomoto, K. 2016, ApJ, 817, 163
Suzuki, T., Zha, S., Leung, S.-C., & Nomoto, K. 2019, ApJ, 881, 64
Takahashi, K., Sumiyoshi, K., Yamada, S., Umeda, H., & Yoshida, T. 2019, ApJ, 871, 153
Takahashi, K., Yoshida, T., & Umeda, H. 2013, ApJ, 771, 28
Timmes, F. X., & Arnett, D. 1999, ApJS, 125, 277
Timmes, F. X., & Woosley, S. E. 1992, ApJ, 396, 649
Toki, H., Suzuki, T., Nomoto, K., Jones, S., & Hirschi, R. 2013, PhRvC, 88, 015806
Tolstov, A., Nomoto, K., Sorokina, E., et al. 2019, ApJ, 881, 35
Tominaga, N., Blinnikov, S. I., & Nomoto, K. 2013, ApJL, 771, L12
Townsley, D. M., Calder, A. C., Asida, S. M., et al. 2007, ApJ, 668, 1118
Walecka, J. D. 1975, in Muon Physics, Volume II: Weak Interactions, ed. V. W. Hughes & C. S. Wu, 114
Walecka, J. D. 1995, Oxford Stud. Nucl. Phys., 16, 1
Wanajo, S., Janka, H.-T., & Müller, B. 2011, ApJL, 726, L15
Wang, R., & Spiteri, R. J. 2007, SIAM J. Numer. Anal., 45, 1871
Zha, S., Chu, M.-C., Leung, S.-C., & Lin, L.-M. 2019, In Preparations